

Dynamics and Stellar Content of the Giant Southern Stream in M31.

I. Keck¹ Spectroscopy of Red Giant Stars

Puragra Guhathakurta², R. Michael Rich³, David B. Reitzel³, Michael C. Cooper⁴,
 Karoline M. Gilbert², Steven R. Majewski⁵, James C. Ostheimer⁵, Marla C. Geha^{6,7},
 Kathryn V. Johnston⁸, and Richard J. Patterson⁵

`raja@ucolick.org, rmr@astro.ucla.edu, reitzel@astro.ucla.edu,`
`cooper@astron.berkeley.edu, kgilbert@astro.ucsc.edu, srm4n@virginia.edu,`
`jostheim@alumni.virginia.edu, mgeha@ociw.edu, kvj@astro.wesleyan.edu,`
`rjp0i@virginia.edu`

ABSTRACT

This paper presents the first results from a large spectroscopic survey of red giant branch (RGB) stars in M31 using DEIMOS on the Keck 10-meter telescope. A photometric pre-screening method, based on the intermediate-width *DDO*51 band centered on the Mg b/MgH absorption feature, was used to select spectroscopic targets. RGB candidates were targeted in a small section of M31's giant southern tidal stream at a projected distance of 31 kpc from the galaxy's center. We isolate a clean sample of 68 RGB stars by removing contaminants (foreground Milky Way dwarf stars and background galaxies) using a combination of spectroscopic, imaging, and photometric methods; the surface-gravity-sensitive Na I doublet is particularly useful in this regard. About 65% of the M31 stars are found to be members of the giant southern stream while the rest appear to be members of the general halo population. The mean (heliocentric) radial velocity of the stream in our field is -458 km s^{-1} , blueshifted by -158 km s^{-1} relative

¹Data presented herein were obtained at the W. M. Keck Observatory, which is operated as a scientific partnership among the California Institute of Technology, the University of California and the National Aeronautics and Space Administration. The Observatory was made possible by the generous financial support of the W. M. Keck Foundation.

²UCO/Lick Observatory, Dept. of Astronomy & Astrophysics, Univ. of California, Santa Cruz, CA 95064

³Dept. of Physics & Astronomy, Univ. of California, Los Angeles, CA 90095

⁴Dept. of Astronomy, Univ. of California, Berkeley, CA 94720

⁵Dept. of Astronomy, Univ. of Virginia, Charlottesville, VA 22903

⁶Carnegie Observatories, 813 Santa Barbara St., Pasadena, CA 91101

⁷Hubble fellow

⁸Van Vleck Observatory, Wesleyan Univ., Middletown, CT 06459

to M31’s systemic velocity, in good agreement with recent velocity measurements at other points along the stream. The intrinsic velocity dispersion of the stream is found to be 15_{-15}^{+8} km s^{−1} (90% confidence limits). A companion paper by Font et al. (2004) discusses possible orbits, implications of the coldness of the stream, and properties of the progenitor satellite galaxy. The kinematics, and possibly the metallicity distribution, of the general halo (i.e., non-stream) population in this region of M31 indicate that it is significantly different from samples drawn from other parts of the M31 halo; this is probably an indication of substructure in the halo. The stream appears to have a higher mean metallicity than the general halo: $\langle[\text{Fe}/\text{H}]\rangle \sim -0.54$ versus -0.74 , and a smaller metallicity spread. The relatively high metallicity of the stream implies that its progenitor must have been a luminous dwarf galaxy. The Ca II triplet line strengths of the M31 RGB stars are generally consistent with photometric estimates of their metallicity (derived by fitting RGB fiducials in the color-magnitude diagram). There is indirect evidence of a population of intermediate-age stars in the stream.

Subject headings: galaxies: M31 — galaxies: kinematics and dynamics — galaxies: abundances

1. Introduction

The growth of galactic halos through the accretion of smaller stellar subsystems has been the subject of many studies over the last few decades (Searle & Zinn 1978; White & Rees 1978). Numerical simulations and semi-analytical modeling of the accretion process have reached new levels of detail in recent years (e.g., Johnston, Hernquist, & Bolte 1996; Johnston 1998; Helmi & White 1999; Helmi & de Zeeuw 2000; Bullock, Kravtsov, & Weinberg 2001). The discovery of the Magellanic Stream (Mathewson, Cleary, & Murray 1974) provided early observational evidence of an ongoing accretion/merger event in the Galaxy involving the Large and Small Magellanic Clouds. The fact that the Magellanic Stream is seen only in neutral hydrogen and not stars has led to some debate over whether ram-pressure stripping or tidal forces are at play (Moore & Davis 1994; Putman, Gibson, & Staveley-Smith 1999; Maddison, Kawata, & Gibson 2002). The best example of an ongoing accretion event in the Milky Way is the Sagittarius dwarf satellite galaxy (Ibata, Gilmore, & Irwin 1994) with its associated tidal debris (Majewski et al. 2003; Newberg et al. 2003). More recently, Sloan Digital Sky Survey (SDSS) stellar density maps have revealed that the low-luminosity, remote star cluster Palomar 5 is undergoing tidal disruption (Odenkirchen et al. 2001; Rockosi et al. 2002). SDSS and Two-Micron All-Sky Survey data have led to the discovery and characterization of the Monoceros stream, an arc-like structure at low Galactic latitude that is probably the result of an encounter with a dwarf galaxy (Yanny et al. 2003; Rocha-Pinto et al. 2003). The Monoceros stream and other Milky Way structures like it are only just being identified: Their large angular extent requires the use of wide-field surveys. Moreover followup studies of these structures can prove to be difficult from our vantage point within the Galaxy’s disk.

In contrast to the Milky Way, its neighbor, the Andromeda spiral galaxy (M31), offers certain advantages for halo studies: Its disk is highly inclined, we have a global external perspective of the galaxy, and yet it is close enough to allow us to characterize the properties of individual stars in detail. Ibata et al. (2001) and Ferguson et al. (2002) present star-count maps covering a large area around M31 and find a giant stream extending to its south (hereafter referred to as the ‘giant southern stream’) along with several other signs of disturbance in the halo and outer disk. While the giant southern stream appears to be tidal debris from a merger event, the origin/nature of the other features is not clear. An investigation of M31’s innermost satellites by Choi, Guhathakurta, & Johnston (2002) confirms the presence of tidally-distorted outer isophotes in NGC 205 and revealed ongoing stripping in M32, with the amount of mass lost estimated to be of the same order as that seen in the stream. However, any association between the stream and M32 (or any other satellite) based on the above studies is largely circumstantial at this point.

Spectroscopy of large samples of individual stars in M31 is the only secure approach to establishing connections between specific streams/features and satellites, and to global mapping of the kinematics and chemical composition of the halo. Reitzel & Guhathakurta (2002, hereafter RG02) carried out spectroscopy of ~ 100 candidate red giant branch (RGB) stars in an outer minor-axis halo field in M31 using the Keck 10-meter telescope and Low Resolution Imaging Spectrograph (LRIS; Oke et al. 1995). Another 150 spectra of M31 RGB candidates in inner minor-axis and outer disk fields are analyzed by Guhathakurta & Reitzel (2002) and Reitzel, Guhathakurta, & Rich (2004). Recent papers by Ibata et al. (2004, see their Figs. 1 and 3) and McConnachie et al. (2004, see their Fig. 3) present radial velocities for several dozen RGB stars in M31. All of these spectroscopic studies taken together have shed light on a variety of topics including the dynamics and metallicity distribution of the M31 halo, the relation between the halo and outer disk, evidence of faint debris trails in the halo, and the orbit of the giant southern stream. There is an important question that remains unanswered though: What fraction of the halo is composed of identifiable streams?

In Fall 2002 we started a spectroscopic survey of the M31 halo with the new Deep Imaging Multi-Object Spectrograph (DEIMOS; Faber et al. 2003) on Keck. This survey has yielded spectra for several hundred RGB candidates to date. The exposures are deep enough to yield information on both radial velocity and spectral absorption features; we consider the latter to be especially important for understanding the formation and evolution of the halo. The broad goals of the project are to characterize the dynamics, chemical abundance distribution, and structure/sub-structure of the M31 halo, with an emphasis on the global statistics and properties of debris trails from past mergers.

In this, the first paper from our DEIMOS survey, we focus our attention on the giant southern stream in M31. Details of the spectroscopic data set on which this paper is based are described in § 2, including target selection, observations, data reduction and verification methods, survey efficiency, success rate of the target selection procedure, and velocity measurement error. The division of our stellar sample into M31 stream RGB, M31 general halo RGB, and foreground Galactic dwarf

populations is described next in § 3. The dynamics of the stream and halo are described in § 4. The metallicity distributions of the stream and general halo are compared in § 5 based on broad-band photometry and spectral absorption features. The main points of the paper are summarized in § 6. The companion paper by Font et al. (2004, hereafter Paper II) uses these and other data to obtain constraints on the orbit of the stream and the nature of the possible progenitor.

2. Data

2.1. Spectroscopic Target Selection

2.1.1. Photometric Pre-Screening of M31 Red Giants

Candidate RGB stars in M31’s giant southern stream were selected from the field ‘a3’ photometry/astrometry catalog of Ostheimer (2002). The catalog is based on Kitt Peak National Observatory (KPNO)¹ 4-meter telescope and MOSAIC camera images in the Washington system M and T_2 bands as well as the intermediate-width $DDO51$ band. Sources were identified and photometered using the DAOPHOT II and ALLFRAME software packages (Stetson 1992, 1994). The photometric transformation relations of Majewski et al. (2000):

$$\begin{aligned} V &= -0.006 + M - 0.200(M - T_2) \\ I &= T_2 \end{aligned} \tag{1}$$

are used to obtain magnitudes on the Johnson/Cousins system (the T_2 band is essentially identical to the I band). The Ostheimer (2002) survey obtained KPNO/MOSAIC data in ten fields around the M31 halo, six of them on the southeast minor axis extending out to $\gtrsim 10^\circ$ from the galaxy center. The observations were carried out before the discovery of the giant southern stream and it is pure chance that field ‘a3’ happens to intersect the stream.

The location of the $35' \times 35'$ field ‘a3’ relative to the stream is shown in Figure 1 (bold square). The field center is located $\xi = +74.8'$ (east) and $\eta = -127.5'$ (south) with respect to M31’s center. Only a portion of the field, the southwest or lower right half, is on the stream: The northeast edge of the stream runs more or less diagonally across field ‘a3’ from northwest to southeast. It should be noted that the surface density of luminous M31 RGB stars is quite low in this remote field, even in the on-stream portion, and there is substantial foreground and background contamination (see § 2.4).

The $DDO51$ filter has a passband of width $\Delta\lambda \approx 100\text{\AA}$ centered at $\lambda \sim 5150\text{\AA}$, designed to include the surface-gravity-sensitive MgI triplet and MgH stellar absorption features (Majewski

¹Kitt Peak National Observatory of the National Optical Astronomy Observatories is operated by the Association of Universities for Research in Astronomy, Inc., under cooperative agreement with the National Science Foundation.

et al. 2000). The features are strong in dwarf stars but weak in RGB stars. Following Palma et al. (2003) each object is assigned a probability of being an RGB star, P_{giant} , based on the degree of overlap of its photometric error ellipse with the (pre-determined) locus of dwarf stars in the $(M - DDO51)$ versus $(M - T_2)$ color-color diagram. The P_{giant} parameter is effective in guiding the selection of RGB stars and in reducing greatly dwarf contamination in the sample, but it is not a perfect discriminant at the relatively faint magnitudes of our survey (as will be shown in § 3.3.3 below): Metallicity variations cause RGB stars to have a relatively broad distribution in two-color space and the few more metal-rich ones that happen to intersect the dwarf locus are assigned a low P_{giant} value; moreover, RGB (dwarf) stars in the tails of the photometric error distribution can scatter close to (far from) the dwarf locus and would then be assigned a low (high) P_{giant} value. Since metallicity is a secondary parameter (after surface gravity) in determining the strength of the Mg b and MgH features, one might worry about DDO51 selection introducing a bias against metal-rich RGB stars. We will examine this issue in § 5.1.2 below and show that such a bias is not important for our sample.

The object detection algorithm in DAOPHOT tends to reject sources that are extended relative to the point spread function but some background field galaxies, especially compact ones, do slip through into the object catalog. The two-color method described above tends to assign high P_{giant} values to galaxies because they are dominated by the light of RGB stars and/or because their Mg b/MgH features are redshifted out of the DDO51 passband making them appear featureless. For this reason the P_{giant} criterion is supplemented by the DAOPHOT-based morphological criteria **chi** and **sharp** to reject galaxies. Naturally, the compact galaxy rejection efficiency of DAOPHOT’s source finding algorithm and **chi/sharp** parameters depends critically on the seeing and depth of the KPNO/MOSAIC imaging data.

2.1.2. Slitmask Design

Three DEIMOS multi-slit masks (#1–#3) were designed for field ‘a3’ using Drew Phillips’ **dsimulator** software (see http://www.ucolick.org/~phillips/deimos_ref/masks.html for details). Table 1 contains a summary of relevant information for the masks. The **dsimulator** software takes as input multiple lists of spectroscopic targets: lists 1, 2, 3, etc., in order of decreasing priority. In addition the targets in each list are assigned weights in direct proportion to their P_{giant} values. The user chooses the mask pointing center and position angle (see thin rectangles in the Fig. 1 inset and Table 1). For each slitmask design the software starts with the highest priority list (list 1) and automatically fills in the $\approx 16' \times 4'$ mask area to the extent possible. It maximizes the sum of weights for the selected targets given two constraints: (i) a minimum length of $6''$ for each slitlet, with the target at least $2.5''$ from each end of the slitlet, and a $0.5''$ gap in the spatial direction between the ends of adjacent slitlets; and (ii) avoidance of inter-CCD gaps and vignetted regions, whose locations within the slitmask are predicted on the basis of an optical model of the spectrograph. Next the software fills in available spaces on the slitmask with targets drawn from

the next input list in the priority sequence (list 2), and so on for lists 3 and 4.

Table 1: Slitmask design parameters and details of observations for the three DEIMOS masks that form the basis of this paper. The number of spectroscopic science targets selected from lists 1–3 for masks #1 and #2 and from lists 1–4 for mask #3 (in order of decreasing priority; see §2.1.2) is indicated; this number does not include alignment stars (list 0). The number of objects is also broken down according to Q , a code indicating reliability of the measured redshift and spectral quality (§2.3.2).

	Mask #1	Mask #2	Mask #3
Pointing center:			
α_{J2000} (h:m:s)	00:48:21.16	00:47:47.24	00:48:23.17
δ_{J2000} (°:′:″)	+39:02:39.2	+39:05:56.3	+39:12:38.5
Position angle (° E of N)	64.2	178.2	270.0
No. of spectroscopic science targets	85	80	83
Breakdown of targets by lists 0/1/2/3/4	5/53/23/9/...	3/54/15/11/...	4/49/17/16/1
Date of observations (UT)	2002 August 16	2002 October 11	2003 October 26
Exposure time (s)	2×1800	3×1800	3×1200
Number of $Q = -2/1/2/3/4$ cases	8/22/14/15/26	6/19/14/9/32	2/0/22/11/48

The mask #1 and #2 designs are each based on three input lists with the following selection criteria:

1. Objects with $20 < I < 22$, $P_{\text{giant}} > 0.5$, $\text{chi} < 1.3$, and $-0.3 < \text{sharp} < +0.3$.
2. Same as list 1 but with the I mag range expanded to $I < 20$ (above RGB tip) and $22 < I < 22.5$ (fainter RGB).
3. Objects with $20 < I < 22.5$, a less stringent $DDO51$ constraint ($P_{\text{giant}} > 0.25$), and slightly less stringent chi/sharp morphology cuts.

After the initial round of observations in Fall 2002, we decided to make some changes to the target selection procedure for our survey in order to fill the slitmasks more efficiently. The design for mask #3 (and the other Fall 2003 masks from our DEIMOS survey that are not presented here) is based on four input lists. The criteria for lists 1 and 2 are the same as those listed above for the first two masks. The list 3 criteria are the same as those listed above except that the P_{giant} requirement is dropped altogether. The list 4 criteria are the same as for the modified list 3 but with further relaxation of the morphology cuts chi/sharp .

The number of spectroscopic targets on masks #1, #2, and #3 is: 85 (53/23/9), 80 (54/15/11), and 83 (49/17/16/1), respectively, where the numbers in parentheses indicate the breakdown by

`dsimulator` input list number. Throughout the rest of this paper we collectively (and loosely) refer to all these targets as “RGB candidates” even though many of them have low P_{giant} values (lists 3 and 4). The slitlet width is set to $1''$. In addition to these science targets, 3–5 bright stars per mask were selected for the purposes of slitmask alignment using the following (list 0) criteria: $I < 20$, same morphology cuts as lists 1 and 2, and no P_{giant} requirement. Each alignment star is assigned a $4'' \times 4''$ box while avoiding overlap with the science target slitlets. After this step `dsimulator` was used to maximize the lengths of all slitlets in the spatial direction while maintaining a $0.5''$ inter-slit separation. A few guide stars were also selected for each mask using the same list 0 criteria as for alignment stars; they are useful for coarse mask alignment and guiding off the TV guider camera, but no spectra are obtained for them.

There are 27 cases of duplication among science targets across the three masks: 15 in common between masks #1 and #2 and 12 in common between masks #2 and #3. No object was observed on all three masks. This level of duplication (15%–20%) was achieved by design; in § 2.5 we estimate the measurement error in radial velocity from these duplicate measurements. The total number of unique M31 RGB candidates targeted across the three slitmasks is 221.

Figure 2 shows a color-magnitude diagram (CMD) of objects in the W portion of field ‘a3’ from which the DEIMOS spectroscopic targets were selected. Extinction/reddening corrections have been applied on a star-by-star basis using the Schlegel, Finkbeiner, & Davis (1998) dust map. The dust is expected to be mostly, if not entirely, in our Galaxy (given that field ‘a3’ is well removed from M31’s disk) so a standard slope of $R_V = 3.1$ is assumed for the extinction law which translates to $E(V - I)/E(B - V) = 1.4$ (Cardelli, Clayton, & Mathis 1989). Panel (a) shows all objects, without any photometric or morphological screening; panel (b) shows only those objects that pass the P_{giant} and morphology cuts for lists 1 and 2. Foreground Galactic dwarf stars in (a) form a broad swath over the color range $0.6 \lesssim (V - I)_0 \lesssim 3$, but the cuts appear to be effective at removing this population at bright magnitudes ($I \lesssim 21$).

2.2. Observations

Masks #1, #2, and #3 were observed on 2002 August 16, 2002 October 11, and 2003 October 26 (UT), respectively, using the Keck II 10-meter telescope and DEIMOS with its $1200 \text{ lines mm}^{-1}$ grating. The exposure times were $2 \times 1800 \text{ s}$, $3 \times 1800 \text{ s}$, and $3 \times 1200 \text{ s}$, respectively. The observational details are given in Table 1. The seeing FWHM was in the range $0.7''$ – $0.9''$. Standard quartz and arc lamp exposures were obtained through each mask for rectification, flat fielding, and wavelength calibration purposes. For details of the instrument we refer the reader to Faber et al. (2003) and <http://alamosana.keck.hawaii.edu/inst/deimos/>.

The mask #1 observation was carried out within two months of the initial commissioning of the DEIMOS spectrograph and even the mask #2 observation was carried out during a period when improvements were continually being made to the instrument; the data are nevertheless of

superb quality. The 28 best stellar spectra, the top third of our 84-star sample in terms of S/N, are presented in Figure 3. The main spectral feature of interest to us is the Ca II triplet at $\lambda \sim 8500\text{\AA}$, although useful information can also be gleaned from other weaker features in this ‘far-red’ region of the spectrum (§ 5.2).

The central wavelength setting was $\lambda 8550\text{\AA}$ for masks #1 and #2. This was changed to $\lambda 7800\text{\AA}$ for mask #3 and the rest of the Fall 2003 masks from our DEIMOS survey (not presented here) to avoid the possibility of losing one of the Ca II triplet lines in the inter-CCD gap and to extend the blue side coverage to the $\lambda 7100\text{\AA}$ TiO and $\lambda 6563\text{\AA}$ H α features. The 1200 lines mm^{-1} grating yields a dispersion of 0.33\AA pix^{-1} and the spatial scale is $0.12''\text{ pix}^{-1}$. The 4×2 array of $2\text{K} \times 4\text{K}$ CCDs span a spectral range of about $\Delta\lambda \gtrsim 2700\text{\AA}$ and a total slitmask length of over $16'$. Thus, spectra from masks #1 and #2 (Fall 2002) cover the range $\lambda\lambda 7200\text{--}9900\text{\AA}$, while mask #3 spectra (Fall 2003) cover $\lambda\lambda 6450\text{--}9150\text{\AA}$. The width of the mask (in the dispersion direction) over which slitlets are distributed is about 2000 pix so the exact spectral coverage varies from slitlet to slitlet by up to a few hundred \AA ; moreover, some spectra are truncated by vignetting (see Fig. 3).

The $1''$ slitlet width used on our masks subtends 4.8 pix, given an anamorphic demagnification factor of 0.57 for the 1200 lines mm^{-1} grating at $\lambda 8500\text{\AA}$. The actual resolution is slightly better than this: For typical seeing of $0.8''$ (FWHM), the spectral resolution is $3.8\text{ pix} = 1.26\text{\AA}$ which corresponds to 44 km s^{-1} or $R \lesssim 7000$ at the Ca II triplet. While this is the characteristic width of stellar absorption lines, the precision with which the centroid of a line can be determined is typically a small fraction of its width. The centroiding accuracy, and hence the radial velocity measurement error (§ 2.5), depends on the S/N ratio or, more specifically, on the significance of the cross-correlation peak (Tonry & Davis 1979).

Prior to starting spectroscopic exposures on each slitmask, we used the mask alignment procedure developed by the DEEP2 team: Guide stars on the TV guider camera were used for coarse alignment; direct images were then obtained through the mask with the grating in zeroth order to fine tune the alignment (both position angle and translation). The procedure converged after 2–3 iterations with typical residuals of $\gtrsim 0.1''$ between the position of the alignment star and the center of its alignment box. This is indicative of the level of astrometric precision in the Ostheimer (2002) catalog from which our spectroscopic targets were drawn.

2.3. Data Reduction

2.3.1. Pipeline Processing

The three DEIMOS masks in field ‘a3’ were processed through the `spec2d` software pipeline (version 1.1.4) developed by the DEEP2 team at the University of California-Berkeley (UCB) for that survey. A brief listing of the main processing steps is given below; details of the data processing steps may be found at <http://astron.berkeley.edu/~cooper/deep/spec2d/primer.html>.

The flat field exposures are used to rectify the curved spectra in the raw spectrogram into rectangular arrays by applying shifts in the spatial direction. Next, a one-dimensional (1D) slit function correction and two-dimensional (2D) flat-field and fringing correction are applied to each slitlet. Using the DEIMOS optical model as a starting point, a 2D wavelength solution is determined from the arc lamp exposures with residuals of order 0.01\AA . Each slitlet is then 2D sky-subtracted exposure by exposure using a B-spline model for the sky. The individual exposures of the slitlet are then averaged with cosmic-ray rejection and inverse-variance weighting. Finally 1D spectra are extracted for all science targets using the optimal scheme of Horne (1986) and converted to plain text format using standard IRAF² tasks.

The 1D spectra shown in Figure 3 represent the top one-third of our stellar sample in terms of S/N: typically $\approx 15\text{\AA}^{-1}$ at the Ca II triplet for this subset. The spectra have been normalized to unit flux at $\lambda 8500\text{\AA}$; they are not flux calibrated and the telluric A-band feature is still present (it will be removed in future versions of the data processing pipeline). Boxcar smoothing, with a 10 pix (3\AA) window and inverse-variance weighting, has been applied to the spectra for illustration purposes.

The DEIMOS spectra presented here are generally of higher quality than the LRIS spectra in the RG02 study, even though the latter typically had $3\times$ longer exposure times (compare Fig. 3 to their Fig. 1). The most significant improvement is Poisson-limited subtraction of the bright night sky emission lines that plague the Ca II triplet region. Improved sky subtraction is the result of three features of DEIMOS: (i) a closed-loop flexure compensation system; (ii) CCDs that lack fringing in the far red; and (iii) a fine enough pixel scale to sample the line spread function well, including the sharp slit edges. Moreover DEIMOS has a higher net throughput than LRIS in this wavelength regime and its spectral coverage is wider than the red side of LRIS. In addition to these improvements in quality, DEIMOS’ roughly $2\times$ larger slitmask area allows a higher degree of multiplexing than LRIS.

The extracted 1D spectra were processed through the `spec1d` pipeline developed for the DEEP2 survey at UCB (an adaptation of the corresponding SDSS pipeline). The pipeline cross-correlates the spectrum of each science target against a series of stellar templates spanning a range of spectral types and emission- and absorption-line galaxy templates to determine the redshift. The science and template spectra are continuum-subtracted and the science spectrum is interpolated to the resolution of the template: $\Delta \log \lambda = 2 \times 10^{-5} \text{pix}^{-1}$. The cross-correlation is computed in pixel space (i.e., real space as opposed to Fourier space) with the relative line strengths and line widths held fixed. The software shifts and scales the template to find the best fit in reduced- χ^2 space. The galaxy templates used in the fitting procedure are linear combinations of the emission- and absorption-line templates whereas the various stellar templates are used individually in the fit. The 10 best solutions for the redshift z of each object are reported, arranged in order of increasing

²IRAF is distributed by the National Optical Astronomy Observatories, which are operated by the Association of Universities for Research in Astronomy, Inc., under cooperative agreement with the National Science Foundation.

reduced- χ^2 .

2.3.2. Quality Assessment

We used the visual inspection software **zspec**, developed by D. Madgwick et al. at UCB for the DEEP2 survey, to view the sky-subtracted 2D and 1D spectra of each slitlet/science target. The extraction window used by the **spec2d** pipeline—i.e., the range of “rows” in the 2D spectrum that are collapsed to form the 1D spectrum—is indicated by markers along the spatial axis of **zspec**’s 2D spectrum display. In rare cases this window appeared to be too narrow/wide or displaced from the target’s stellar continuum (or emission lines); we manually set the extraction window in these cases, re-extracted the 1D spectrum, and processed it through **spec1d** pipeline.

The 10 best redshift choices from **spec1d** are listed by **zspec**. Selecting one of the z choices causes the corresponding (appropriately redshifted) template to be displayed overlaid on the science target’s 1D spectrum. The positions of prominent absorption or emission lines in the template in question (e.g., Ca II triplet lines for a stellar template and [O II], [O III], H β , etc. lines for an emission-line galaxy template) are marked on the 1D and 2D spectra. The night sky spectrum, or more precisely the variance versus wavelength, is plotted along side the target’s 1D spectrum; it proved to be very useful in deciding which spectral features were reliable and which ones were not. Different degrees of smoothing were tried on the target’s 1D spectrum to enhance the S/N at the cost of spectral resolution—this afforded a better view of its spectral features and allowed us to assess the reality of marginal/weak ones.

For about half the targets from masks #1 and #2 and two-thirds of those from mask #3 it was easy to pick out the correct z value from the choices provided by **spec1d**. On rare occasions, none of the 10 choices was accurate but it was obvious from the 1D spectrum what the correct z was. The redshift was marked *manually* in these cases. It was typically based on the Ca II triplet, often a subset of the three lines (the reddest line lies amidst a cluster of night sky lines and is sometimes affected by them), the $\lambda 7100\text{\AA}$ TiO band (for red stars), and/or the Na I doublet (dwarf stars). Only 19 out of the 248 science targets, or 17 out of the 221 unique M31 RGB candidates (8%), are in this “ z -by-hand” category.

Following the classification scheme used in the DEEP2 survey (Coil et al. 2004), each science target was assigned a quality code Q to indicate the reliability of the measured redshift and the overall quality of its spectrum. The above cases with well-measured z ’s, including the “ z -by-hand” cases, were placed in one of two categories: (i) $Q = 4$ for redshifts based on two or more robust spectral features; and (ii) $Q = 3$ for those based on one robust feature and one or more marginal ones or on a few marginal features. The $Q = 4$ z measurements are expected to be “rock solid” with something like 99% confidence, whereas the $Q = 3$ z ’s are expected to have $\gtrsim 90\%$ reliability. No distinction is made between $Q = 3$ versus $Q = 4$ cases in the rest of this paper; both are treated as secure redshifts.

Objects for which the redshift measurement failed fall into three categories designated: (i) $Q = -2$ to indicate a catastrophic failure in the data reduction for instrumental reasons such as severe vignetting, the spectrum landing in the inter-CCD gaps, near the periphery of the CCD array, or on a bad column, poor sky subtraction, scattered light problems, etc.; (ii) $Q = 1$ for slitlets with a barely visible spectral continuum and/or very low S/N; and (iii) $Q = 2$ for cases where the S/N is marginal to adequate but there is not enough information for reliable z determination. Judging from the DEEP2 survey, some of our $Q = 2$ cases are probably distant red galaxies for which the limited spectral coverage and low S/N prevent us from making a reliable redshift measurement. The low S/N in some of the $Q = 1$ cases in our sample, especially the handful of bright ones [Fig. 2(c)], could be the result of early mask design/fabrication problems. Such instrumental failures rightfully belong in the $Q = -2$ category, but we have not attempted to reclassify any $Q = 1$ cases as there is no direct way to confirm this hypothesis.

A heliocentric correction is applied to each of the three masks using the IRAF task RVCOR. The observation dates span a wide range and the corrections span a range as well: $+23 \text{ km s}^{-1}$ (mask #1), $+4 \text{ km s}^{-1}$ (mask #2), and -3 km s^{-1} (mask #3).

2.4. Efficiency / Success Rate

In this section we assess the efficiency of our spectroscopic survey and success rate of the photometric target selection procedure—i.e., the yield of M31 RGB stars. We do this by counting up the numbers of objects from all three masks in the different redshift quality (Q) code categories.

Starting with the failed z measurements, the number of $Q = -2/1/2$ cases is 8/22/14, 6/19/14, and 2/0/22 for masks #1, #2, and #3, respectively (Table 1). Most of the 16 catastrophic failures ($Q = -2$) are near the ends of the masks and there are as many as 7 duplicates among them; this high duplicate fraction (nearly 50%) is attributable to the fact that the overlap between masks occurs only near their ends (Fig. 1).

The fraction of catastrophic failures is lower for the Fall 2003 mask #3 than for the Fall 2002 masks #1 and #2, and the fraction of spectroscopic successes higher. There are a few reasons for this. The Fall 2002 mask designs were based on a preliminary optical model for the spectrograph in `dsimulator`: Design imperfections resulted in some slitlets on masks #1 and #2 being affected by vignetting and inter-CCD gaps. The DEIMOS optical model was refined in time for the Fall 2003 mask designs. The procedure for taking proper calibration data to achieve good wavelength calibration and flat-fielding was fine-tuned over the course of a few months by the DEEP2 and DEIMOS teams, so the calibration is less than ideal for the two early masks. The Fall 2002 wavelength setting was not optimal in that there was a finite chance of one of the three Ca II triplet lines landing in the inter-CCD gap; the wavelength setting was improved for the Fall 2003 observations. Finally, the observing conditions were slightly sub par for the two early masks with occasional thin cirrus and/or worse-than-average seeing.

It is noteworthy that there is no significant difference in success rate between masks #1 and #2 even though the integration time is 50% longer for the latter. This suggests that factors other than total exposure time (e.g., such as the factors listed above) are responsible for determining the final data quality and success rate for the two early masks.

There are 9 catastrophic failures ($Q = -2$) among the 221 unique RGB candidates targeted on the three masks. While these failures lower the overall efficiency of our survey, it is important to keep in mind that they are *instrumental* failures that reflect in no way on the physical properties of the targeted objects or on the success rate of the photometric screening procedure—i.e., it is as though these objects were not observed at all. For this reason, the percentages quoted below are measured relative to a denominator of 212 objects ($= 221 - 9$), those for which spectra were successfully obtained.

The number (percentage) of $Q = 1$ and 2 cases is 38 (18%) and 46 (22%), respectively. Among the remaining 128 objects (60%) with definite redshifts, there are 44 galaxies (21%), mostly compact emission-line galaxies, spanning the redshift range $z = 0.1$ – 1.5 . That leaves 84 stars (39%), of which 68 (32%) are M31 RGB stars and 16 (7.5%) are foreground Galactic dwarf stars, as we will show in § 3.3. The efficiency and success rate for the rest of our DEIMOS survey are expected to be higher than the fractions quoted here: Most of the remaining slitmasks (i.e., those not presented in this paper) were observed in Fall 2003 and should therefore be comparable to mask #3.

It is instructive to examine the foreground/background contamination rates in the present study in the context of the earlier RG02 survey. The surface density of M31 stars at the $R = 31$ kpc location of our field ‘a3’ (including the contribution of the giant southern stream) should be roughly similar to that in RG02’s $R = 19$ kpc minor-axis field; the surface density of foreground Galactic stars and background field galaxies is also expected to be the same in the two fields. Milky Way dwarf stars constituted an estimated 57% of RG02’s sample of 80 stars, whereas they represent only 16 out of the 84 stars (19%) in the present study, or 6 out of 62 stars (10%) if one excludes the “filler” targets (lists 3 and 4) for which the P_{giant} criterion was relaxed or dropped. The suppression of foreground contaminants in our study is attributable to *DDO51*-based pre-selection of spectroscopic targets (§ 2.1). Spectroscopically-confirmed galaxies comprise about a fifth of our sample of 212 targets, but the true galaxy contamination rate could easily be higher by a factor of two since some (unknown) fraction of the $Q = 2$ cases (and possibly $Q = 1$ cases) are probably background galaxies. The efficiency with which the morphological criteria **chi/sharp** reject compact galaxies is very sensitive to the seeing and depth of the KPNO/MOSAIC image; there is a fair bit of variation in seeing/depth across the different fields in the Ostheimer (2002) survey. The RG02 study had a lower galaxy contamination rate (estimated to $\sim 10\%$) thanks to their use of four-band photometry to pre-screen against galaxies and better seeing.

2.5. Velocity Measurement Error

The 27 duplicate measurements across the three masks include 13 cases where both members of the pair are secure z determinations ($Q = 3$ or 4): 8 stars, 3 emission-line galaxies, and 2 absorption-line galaxies. The rms radial velocity difference between pairs of measurements for the 8 stars is $21 \pm 5 \text{ km s}^{-1}$. The $\pm 1\sigma$ uncertainty in the rms estimate was derived from 1000 sets of 8 Monte Carlo drawings from a Gaussian distribution. Assuming the measurement uncertainty is the same for each member of the pair, the radial velocity error for an individual measurement is $\sqrt{2}$ times smaller than the rms of the difference, or $15 \pm 3.5 \text{ km s}^{-1}$. The velocity error is probably smaller for mask #3 than for the other two masks, but this is ignored in the above estimate. We will use this velocity error estimate in § 4.1.3 to constrain the coldness of the stream.

The overlap areas between masks, where we have duplicate observations, are located near the ends of the masks (Fig. 1) and the data quality appears to be sub-optimal in these regions (§ 2.4). This provides a plausible explanation for the fact that 5 of the 16 duplicate star measurements (31%) are “ z -by-hand” cases, whereas only 13% of all secure z determinations are in this category. The velocity measurement error for the typical star in our sample is likely to be somewhat smaller than the above estimate of 15 km s^{-1} .

3. Sorting Out the Stellar Sample

In this section, we describe how the 84 confirmed stars in our sample are sorted into three groups: (i) RGB stars in M31’s giant southern stream; (ii) RGB stars belonging to M31’s general halo population; and (iii) foreground Galactic dwarf stars. The surface density of luminous RGB stars is relatively low at the location of our field ‘a3’, in the outer halo of M31 at a projected distance of $R = 31 \text{ kpc}$ from the center of the galaxy close to its minor axis. Despite the $\approx 3\times$ overdensity due to the presence of the stream (§ 3.2) and the use of *DDO51* photometry to screen out Milky Way dwarf stars (§ 2.1), our spectroscopic sample contains a non-negligible fraction of foreground dwarf star (and background field galaxy) contaminants. We demonstrate below that a few key pieces of photometric and spectroscopic information can be used to distinguish between stream and general halo populations and to eliminate all contaminants from our field ‘a3’ sample without any significant loss of M31 RGB stars. The radial velocity distribution of stars is a logical starting point for this analysis.

3.1. Line-of-Sight Velocity Distribution

Figure 4 shows radial velocity histograms for stars in our field ‘a3’ spectroscopic sample, first slitmask by slitmask and then for the combined sample of 84 unique objects. Three features of the distribution are worthy of note: (i) a strong and narrow peak that dominates each of

the four histograms and presumably corresponds to M31’s giant southern stream; (ii) a low-level broad component that is shifted towards less negative velocities than the main peak ($-500 \lesssim v < -200 \text{ km s}^{-1}$); and (iii) a weak concentration of stars seen as a disjoint group in the range $-150 \lesssim v < 0 \text{ km s}^{-1}$. A two-Gaussian maximum likelihood fit to the first two components is shown as a thin solid line in panel (d). We will show below that the second component represents M31’s general halo population (§ 4.2) while the third consists of Galactic dwarf stars along the line of sight, but well in front of M31 of course (§ 3.3).

Mask #3 has the highest success rate of the three masks for reasons discussed in § 2.4: Their velocity histograms contain 26, 27, and 39 stars, respectively, even though the number of spectroscopic targets on the three masks is comparable. The foreground dwarf star fraction is highest in the mask #3 velocity histogram because the P_{giant} criterion was dropped entirely while selecting lists 3 and 4 “filler” spectroscopic targets (see § 2.1.2).

3.2. Contrast of Stream Against Smooth Halo

The two-Gaussian fit indicates that the ratio of giant southern stream to general halo stars is about 45:23—i.e., that the stream comprises $65^{+12}_{-21}\%$ (90% confidence limits from the maximum likelihood analysis) of the M31 population in field ‘a3’. The actual ratio of stream to general halo stars may be somewhat higher than this: The $I < 22.5$ limiting magnitude, and possibly the *DDO*51 criterion, used in the spectroscopic target selection process tends to bias the sample against the most metal-rich RGB stars and these stars constitute a larger fraction of the stream than the general halo population (§ 5).

It is important to note that we can only distinguish between stream and general halo stars on a statistical basis. The radial velocity range over which the stream dominates, $v < -410 \text{ km s}^{-1}$, contains 47 stars of which 45 are estimated to be members of the stream while the remaining two are members of the halo. The 21 M31 RGB stars outside this velocity range are all likely to be members of the halo.

The surface density of the stream appears to be roughly constant along its length over a wide range (see star count map in Ferguson et al. 2002). Since the halo density falls monotonically with increasing distance from the galaxy center, the contrast of the stream is expected to become progressively stronger. This is evident from the velocity histograms presented in the Ibata et al. (2004) study (compare fields 1, 2, 6, and 8 in their Fig. 1); in fact, the contrast in their innermost field (field 8) is so low that the stream is not readily discernible as a distinct population. It should be noted that the Ibata et al. fields were chosen to run along the highest surface density part of stream whereas our field ‘a3’ sample is drawn from the edge of the stream (by chance), so the stream-to-general halo ratio in their fields should be slightly higher than in ours at the same radial distance from M31.

3.3. Rejecting Foreground Galactic Dwarf Stars

This section discusses foreground Milky Way dwarf star contaminants in our sample. Galaxies with high quality spectra ($Q = 3$ or 4) are easily identified on the basis of redshift and spectral characteristics and removed from the sample, but it is a little more difficult to screen out foreground dwarf stars. Five pieces of information can be used to distinguish M31 RGB stars from foreground Galactic dwarfs: (i) radial velocity, (ii) location within the $(V - I, I)$ CMD, (iii) P_{giant} parameter derived from the $(M - DDO51)$ versus $(M - T_2)$ two-color diagram, (iv) strength of the $\lambda 8190\text{\AA}$ Na I doublet in red (cool) stars, and (v) comparison of photometric versus spectroscopic metallicity estimates. In general, no single criterion of the five is by itself a perfect discriminant between RGB and dwarf stars, but the combination is very effective. We discuss each of these criteria in turn below.

3.3.1. Radial Velocity

The radial velocity histogram of the combined stellar sample [Fig. 4(*d*)] has a distinct *gap* separating a group of 68 stars with $v < -200 \text{ km s}^{-1}$ from a group of 16 stars with $v > -150 \text{ km s}^{-1}$ (shaded histogram). The former group of stars includes the prominent peak associated with the giant southern stream and is roughly centered on M31’s systemic velocity of -300 km s^{-1} ; they are therefore designated ‘candidate M31 RGB stars’. The latter group of stars occupies the radial velocity range predicted by the IASG Galactic star-count model (RG02; Bahcall & Soneira 1984; Ratnatunga & Bahcall 1985); they are therefore designated ‘candidate Galactic dwarf stars’. We will now test the validity of these designations by comparing the properties of these two groups of stars.

3.3.2. Color-Magnitude Diagram

The CMD locations of the two subgroups of stars are consistent with the above designations. Candidate M31 RGB stars have a distribution that is nicely bracketed by the model RGB tracks [Fig. 2(*d*)] with the majority lying below the RGB tip (the few exceptions will be discussed in § 5.1.3). By contrast very few candidate Galactic dwarfs lie below the RGB tip [Fig. 2(*c*)]—this is not surprising because the density of Milky Way (thin and thick disk) stars is on the decline at these faint apparent magnitudes and the probability of including a foreground dwarf star is further diminished by the onset of M31’s RGB [see Figs. 2(*a–b*)].

3.3.3. *DDO51-Based Selection*

A feature of our DEIMOS spectroscopic survey that sets it apart from previous studies of M31 is *DDO51*-based pre-screening of RGB stars (§ 2.1). Figure 5 shows a plot of P_{giant} versus radial velocity for the 84 stars in our sample. As expected the majority of candidate Galactic dwarfs (10 out of 16) have $P_{\text{giant}} < 0.5$, even though only a small fraction of the total number of spectroscopic targets are below this cut: only 37 “filler” targets (lists 3 and 4) out of a total of 248 targets on the three masks or 15% (Table 1). By contrast most candidate M31 RGB stars are above the cut (62 out of 68, or 90%). Put another way, the ratio of candidate M31 RGB to Galactic dwarf stars is 62:6 for $P_{\text{giant}} > 0.5$, and 6:10 for $P_{\text{giant}} < 0.5$. This demonstrates the usefulness of *DDO51*-based pre-screening for improving the yield of RGB stars. However, while candidate M31 RGB stars have a higher mean/median P_{giant} value than candidate Galactic dwarfs (consistent with their designations), the distributions are broad and overlap each other so that there is not a clear separation between the two populations.

3.3.4. *Sodium Doublet Line Strength*

Spinrad & Taylor (1969) first developed the use of the $\lambda\lambda 8183, 8195\text{\AA}$ Na I absorption line doublet as a surface-gravity indicator. More recently Schiavon et al. (1997) have shown that the Na I doublet is expected to be strong in dwarf stars cooler than $T_{\text{eff}} \sim 4000\text{ K}$, which corresponds to $(V - I)_0 > 1.8$ according to the calibration relation of Alonso, Arribas, & Martínez-Roger (1999), while RGB stars and hotter dwarfs are expected to have weak lines. We test this diagnostic on the sample of 84 stars in field ‘a3’.

Figure 6 is a plot of the Na I doublet equivalent width $\text{EW}(\text{Na})$ as a function of the dereddened broadband color $(V - I)_0$ for our stellar sample. The $\text{EW}(\text{Na})$ computation is done within a window of width $\Delta\lambda = 21\text{\AA}$ centered on $\lambda 8190\text{\AA}$ with continuum bands of roughly twice/half the width on the blue/red sides; this is a departure from the Na index definition of Schiavon et al. (1997), which is inevitable since our spectra have much lower resolution than theirs, but should be fine for an assessment of the *relative* line strengths of RGB versus dwarf stars. The error $\sigma[\text{EW}(\text{Na})]$ is assumed to scale inversely with S/N and is estimated empirically from the 8 stars with duplicate measurements. Red stars display a bimodal distribution of Na I line strengths as expected. It is very reassuring that our velocity-based subsamples track this bimodality. The high S/N cases with $(V - I)_0 > 1.8$ in Figure 6 best demonstrate this: Candidate M31 RGB stars (circles) lie at or below the $\text{EW}(\text{Na}) = 1.8\text{\AA}$ threshold (dashed horizontal line) while candidate Galactic dwarfs (crosses) lie at or above it.

3.3.5. Calcium Triplet Line Strength

The final criterion for distinguishing candidate M31 RGB stars from candidate foreground Galactic dwarfs is a comparison between photometric and spectroscopic metallicity estimates. The $[\text{Fe}/\text{H}]_{\text{phot}}$ estimate is derived from the position of the star in the CMD relative to model RGB tracks (see § 5.1.1 below). The $[\text{Fe}/\text{H}]_{\text{spec}}$ estimate is derived from the strength of the Ca II absorption line triplet and empirical calibration relations based on RGB stars in Galactic globular clusters (§ 5.2.1). RG02 found that M31 RGB stars lie close to the $[\text{Fe}/\text{H}]_{\text{spec}} = [\text{Fe}/\text{H}]_{\text{phot}}$ line, whereas Galactic dwarfs have weaker Ca II lines so that $[\text{Fe}/\text{H}]_{\text{spec}} < [\text{Fe}/\text{H}]_{\text{phot}}$ for the most part (see their Figs. 13 and 14). We will show in Figure 12 and § 5.2.3 below that the Ca II triplet line strengths measured in coadded spectra of M31 RGB stars and Galactic dwarfs in our field ‘a3’ sample follow these same trends.

3.3.6. Discussion: Towards a Clean and Complete Sample of M31 Red Giant Stars

Of the five diagnostics discussed above, the Na I doublet is the most powerful for foreground dwarf rejection. Based on the (admittedly arbitrary) color and $\text{EW}(\text{Na})$ thresholds in Figure 6 (dashed lines), there are 10 and 19 stars in the top right and bottom right sections which should be considered definite Galactic dwarfs and definite M31 RGB stars, respectively. All 29 stars were required to be well measured, $\sigma[\text{EW}(\text{Na})] \lesssim 1\text{\AA}$, and to be separated by at least $1.5\sigma[\text{EW}(\text{Na})]$ from the horizontal line. The Na I doublet feature is easily visible for the 10 definite dwarfs in Figure 3 (marked by triangles). The definite dwarfs and definite RGB stars are marked as crosses and filled circles, respectively, in Figure 5. It is very reassuring that these two subgroups maintain perfect separation in radial velocity—in other words, none of the candidate Galactic dwarfs turned out to be a definite M31 RGB star and vice versa.

It is worth checking whether *any* of the 16 candidate foreground Galactic dwarfs might actually be M31 RGB stars. With this in mind, we examine their properties using Figures 2, 5, and 6, going through the subsample one star at a time trying to identify possible RGB interlopers:

- Obviously, the 10 cool stars that lie well above the $\text{EW}(\text{Na})$ threshold are definite dwarfs. It is useful to check how they fare with respect to some of the other diagnostics. All 10 lie at or above M31’s RGB tip in the CMD. Three of them have $P_{\text{giant}} \gtrsim 0.7$, two have $P_{\text{giant}} \approx 0.4$, and five have $P_{\text{giant}} < 0.1$, again emphasizing that the P_{giant} parameter is not a perfect discriminator between dwarfs and RGB stars.
- The candidate cool dwarf at $(V - I)_0 = 1.98$ appears to have a strong Na I doublet feature, $\text{EW}(\text{Na}) = 3.19\text{\AA}$, but its spectrum is so noisy that its offset above the threshold corresponds to only $1\sigma[\text{EW}(\text{Na})]$. In other words, the Na test suggests that it is a dwarf but is not definitive. The object lies well below M31’s RGB tip in the CMD. Its relatively low P_{giant} value of 0.35 tips the scale in favor of a Galactic dwarf classification.

- Two candidate dwarfs lie close to the $\text{EW}(\text{Na})$ threshold, one 0.5 mag redder than the color cut and the other 0.2 mag bluer than it. Even though the Na diagnostic is inconclusive, they are both likely to be dwarfs based on two other factors: (i) relatively small P_{giant} values—0.41 and 0.09, respectively; and (ii) CMD locations close to M31’s RGB tip.
- The candidate dwarf with $(V - I)_0 = 1.46$ and $\text{EW}(\text{Na}) = 0.65\text{\AA}$ is too hot for the Na test to be used. It is about 1 mag fainter than M31’s RGB tip and has a relatively high P_{giant} value, 0.63. These factors suggest that the object may be an M31 RGB star.
- Finally, two candidate dwarfs lie within ≈ 0.1 mag of the color cut but on the blue side. Both have noisy spectra but appear to lie significantly below the threshold if our empirical scaling of $\sigma[\text{EW}(\text{Na})]$ is to be trusted. It is intriguing that the two have relative large P_{giant} values, 0.54 and 0.86, and both lie ≈ 1 mag below the tip of M31’s RGB in the CMD. Like the last star, these two should also be considered possible M31 RGB stars.

In summary, there are three stars among the 16 velocity-selected candidate dwarfs that could be M31 RGB stars. All three are relatively faint and do not have well measured photometric and spectroscopic parameters as a result. None of the three present a strong/definite enough case to warrant reclassification at this stage. We will return to a discussion of these objects in § 4.2.

We next use similar reasoning to test whether *any* of the 68 candidate M31 RGB stars might actually be foreground Galactic dwarfs:

- The 48 candidate M31 RGB stars with $v < -400 \text{ km s}^{-1}$ can be ruled out as potential dwarfs on the basis of the IASG Galactic structure model (Bahcall & Soneira 1984; Ratnatunga & Bahcall 1985) which predicts that the foreground dwarf contamination rate should be negligible at these large negative radial velocities (see Fig. 5 of RG02). The giant southern stream population should be completely free of foreground dwarf contamination by virtue of its large blueshift.
- The remaining 20 candidate M31 RGB stars in the radial velocity range $-400 < v < -200 \text{ km s}^{-1}$ all have $P_{\text{giant}} \gtrsim 0.6$ so are unlikely to be dwarfs.
- The Na diagnostic does not turn up any compelling evidence to suggest that there dwarf interlopers among this sample of 20. Twelve are to the left of the color cut and eight are to the right of it. None of the 20 are significantly above the $\text{EW}(\text{Na})$ threshold; six are significantly below it, three on each side of the color cut.

In summary, there is nothing to suggest that any of the candidate M31 RGB stars requires reclassification.

Given the clean RGB versus dwarf star distinction provided by the Na I doublet diagnostic in Figures 5 and 6, coupled with all the earlier evidence, it is probably safe to drop the term

“candidate” from the designations: Unless otherwise mentioned, we refer to the $v < -200 \text{ km s}^{-1}$ group as M31 RGB stars and the $v > -150 \text{ km s}^{-1}$ group as Galactic dwarfs throughout the rest of this paper.

3.3.7. Comparison to Earlier Studies

Previous spectroscopic studies of M31 stars have adopted a more limited approach to RGB versus dwarf star discrimination. None of these studies had access to *DDO*51 photometry that is so valuable for suppressing foreground dwarf contamination in our DEIMOS survey. RG02 used radial velocities, CMD information, and the $[\text{Fe}/\text{H}]_{\text{spec}}$ versus $[\text{Fe}/\text{H}]_{\text{phot}}$ comparison; the resulting RGB/dwarf star separation was not as clear as in this study. The Reitzel et al. (2004) study used radial velocities alone, while Ibata et al. (2004) made no mention of foreground contamination; neither of these last two studies made use of spectral absorption line strengths.

4. Dynamics

The dynamics of the giant southern stream and general halo (non-stream) populations in M31 are described in this section. A maximum likelihood fit of the sum of two Gaussians is carried out on the radial velocity distribution of the 68 M31 RGB stars. This is used to characterize the mean velocity and velocity dispersion of the two components. Figure 7 shows $\Delta\chi^2$ ($\equiv \chi^2 - \chi_{\text{min}}^2$) curves for these four quantities (four of the five parameters in the fit); the optimal value of each parameter and uncertainty, in the form of 90% confidence limits, are indicated.

4.1. Giant Southern Stream

4.1.1. Mean Radial Velocity

The taller/narrower of the two Gaussians in the maximum likelihood fit corresponds to the main peak in the stellar radial velocity distribution [Fig. 4(*d*)]. Based on this fit, we determine that the giant southern stream has a mean heliocentric radial velocity of $-458 \pm 6 \text{ km s}^{-1}$ (90% confidence limits), or a line-of-sight velocity of -158 km s^{-1} with respect to M31 [see Fig. 7(*a*)]. Our measurement is consistent with recent measurements by Lewis et al. (2004) and Ibata et al. (2004) at other points along the stream in the sense that our field ‘a3’ lies between their fields 2 and 6 both in terms of sky position and radial velocity. The companion Paper II uses the field ‘a3’ mean velocity from this study, along with other velocity data (Lewis et al. 2004; Ibata et al. 2004) and line-of-sight distance estimates (McConnachie et al. 2003), to constrain the orbit of the stream and its progenitor satellite.

4.1.2. Velocity Gradients

We next explore possible trends in the mean velocity of M31’s giant southern stream as a function of sky position. Figure 8 shows the radial velocity distribution of M31 RGB stars as a function of projected position along and perpendicular to the stream (top and bottom, respectively). The positions are defined relative to the center of field ‘a3’ with Δr_{\parallel} increasing from northwest to southeast and Δr_{\perp} increasing from southwest to northeast; in other words, the projection of the stream is assumed to be at a position angle of -45° (Fig. 1). We conclude that there is no strong velocity gradient along either axis. The dashed lines in Figure 8 mark the nominal slopes, $dv/dr_{\parallel} = -0.5 \text{ km s}^{-1} \text{ arcmin}^{-1}$ and $dv/dr_{\perp} = +0.6 \text{ km s}^{-1} \text{ arcmin}^{-1}$, but there is uncertainty about the membership of any given RGB star (stream versus general halo; see §3.2) and large Poisson errors. As discussed in Paper II, our measurement of the local velocity gradient along the stream in field ‘a3’ is consistent with the published radial velocities over a longer spatial baseline (Lewis et al. 2004; Ibata et al. 2004).

Any systematic trend in the stream’s mean velocity with position tends to broaden the peak in the velocity histogram. The radial velocity gradient along the direction parallel to the stream is $dv/dr_{\parallel} = -0.47 \text{ km s}^{-1} \text{ arcmin}^{-1}$ so this translates to a spread of $\Delta v = \pm 4.7 \text{ km s}^{-1}$ over the $\Delta r_{\parallel} \sim 20'$ spanned by our three masks along the length of the giant southern stream (see Figs. 1 and 8). This spread is small compared to the width of the peak associated with the stream. Indeed we have checked explicitly that correcting for the gradient has a negligible effect on the width of the best-fit Gaussian.

4.1.3. Intrinsic Velocity Dispersion

Figure 7(b) shows the likelihood function for the width of the Gaussian corresponding to the giant southern stream. The best-fit width is $\sigma_v^{\text{stream}} = 21 \pm 7 \text{ km s}^{-1}$ (90% confidence limits). The 1σ velocity measurement error of 15 km s^{-1} (§2.5) is subtracted in quadrature from the measured velocity dispersion of the stream. Our best estimate of the *intrinsic* line-of-sight velocity dispersion of the stream is $\sigma_v^{\text{stream}}(\text{intrinsic}) \approx 15 \text{ km s}^{-1}$ but, given the large uncertainty in the measured value, we conclude that $\sigma_v^{\text{stream}}(\text{intrinsic}) \lesssim 23 \text{ km s}^{-1}$ (90% confidence limit). This is comparable to the velocity dispersions measured in the Milky Way’s Monoceros and Sagittarius streams (Crane et al. 2003; Majewski et al. 2004a). We consider the coldness of the stream and its implications in Paper II.

4.2. General Halo (Non-Stream) Population: Evidence of Substructure

In this section we turn our attention to the kinematics of M31’s general halo (i.e., non-stream) population. The broad, low-level component in the combined stellar radial velocity histogram

[Fig. 4(*d*)] spans the range $-500 \lesssim v < -200 \text{ km s}^{-1}$ and extends to the right of the main peak. As we will show in §5.1.3 below this component has a large spread in $[\text{Fe}/\text{H}]$ comparable to that seen in other studies of the halo (even though there are differences in detail). The broad component is *not* merely the tail of the giant southern stream’s radial velocity distribution judging from the differences in their stellar populations: The former appears to be more metal poor, has a larger metallicity spread, and lacks stars above the RGB tip (see §5.1.3 and Figs. 2 and 10).

The broader of the two components in the maximum likelihood fit to the radial velocity distribution of M31 RGB stars is centered at a heliocentric velocity of $-333_{-51}^{+33} \text{ km s}^{-1}$ and has a Gaussian width of $65_{-21}^{+32} \text{ km s}^{-1}$ [90% confidence limits; see Fig. 7(*c-d*)]. The broad halo component appears to be adequately fit by a Gaussian but the large Poisson fluctuations (only ≈ 21 stars belong to this component) make it impossible to tell whether its radial velocity distribution is drawn from a truly smooth and virialized underlying distribution or if it contains substantial substructure.

The velocity distribution of the general halo population in field ‘a3’ appears to be anomalously narrow. Its width $\sigma_v^{\text{halo}}(\text{field ‘a3’}) = 65_{-21}^{+32} \text{ km s}^{-1}$ is significantly smaller than the width of $\sigma_v^{\text{halo}}(\text{other}) = 150 \text{ km s}^{-1}$ measured for other M31 halo tracers: field RGB stars in an $R = 19 \text{ kpc}$ minor-axis field (RG02) and global samples of globular clusters and planetary nebulae (see Evans & Wilkinson 2000, and references therein). A plausible explanation of this is that our field ‘a3’ sample is dominated by substructure in the halo—e.g., it consists of one or two subclumps instead of a smooth, virialized distribution. This is the first of three lines of evidence pointing to the possible existence of substructure in the general halo population in this remote M31 field.

We next consider the three possible M31 RGB interlopers among the 16 stars with $v > -150 \text{ km s}^{-1}$ (candidate Galactic dwarfs) that have been excluded from the dynamical analysis so far (see bullets in §3.3.6). Their radial velocities, -21 , -127 , and -18 km s^{-1} , place them right among the foreground Galactic dwarf population, but it is possible that they belong to the M31 halo instead: For example, they would be within $3\sigma_v^{\text{halo}}$ of a broad distribution centered on M31’s systemic velocity of -300 km s^{-1} . Including all three as members of the M31 halo changes the best-fit width to $\sigma_v^{\text{halo}} = 116_{-22}^{+31} \text{ km s}^{-1}$, while including only the last pair of stars as halo members (probably more realistic) changes the width to $\sigma_v^{\text{halo}} = 103_{-21}^{+28} \text{ km s}^{-1}$, where the quoted uncertainties are 90% confidence limits derived from new maximum likelihood fits in each case. Our basic conclusion about the field ‘a3’ halo sample having an unusually narrow velocity distribution seems to be independent of whether or not the possible RGB interlopers are included in the sample.

The centroid of the radial velocity distribution of the halo population is offset by -33 km s^{-1} with respect to M31’s systemic velocity of -300 km s^{-1} , and the offset is significant at the 90% confidence level, based on the maximum likelihood fit to the primary sample of 68 M31 RGB stars (possible interlopers excluded). Inclusion of the possible interlopers leads to a small shift in the best-fit halo mean velocity towards less negative values and a reduction therefore in the magnitude of the offset relative to systemic, along with a slight increase in the uncertainty: The net result of these changes is the best-fit offset of -19 km s^{-1} is no longer statistically significant. If the

observed offset is real/significant, it could be a second sign of substructure in M31’s halo. A third possible sign of substructure is the apparent difference between the metallicity distributions of the field ‘a3’ halo sample and RG02’s sample (see § 5.1.3 below).

An alternative explanation of the observed velocity offset (taken at face value) is that it is a result of global rotation of M31’s halo. The sense of halo rotation would then be the same as for M31’s disk whose southwest half is known to be blueshifted relative to systemic. Since our field ‘a3’ lies close to the minor axis, this would imply that we are seeing only a small component of the full halo rotation speed and would therefore place a lower limit of $(v_{\text{rot}}/\sigma_v)^{\text{halo}} \gtrsim 0.2$. The M31 halo appears to have an aspect ratio of 5:3 (in projection) judging from the isopleths in the Ibata et al. (2001) star-count map. If the observed flattening is due to halo rotation, this would require $(v_{\text{rot}}/\sigma_v)^{\text{halo}} \sim 0.8$ (Binney & Tremaine 1987) which is consistent with our lower limit. If M31’s halo is confirmed to be rotating at this level, it would be in stark contrast to the Milky Way halo which appears to have little or no (or even slight retrograde) rotation (Majewski 1992; Majewski, Munn, & Hawley 1996; Popowski & Gould 1998).

In closing, we note that there are very few constraints on the global dynamics of M31’s stellar halo at the present time. Only two sight-lines have been probed using field RGB stars—field ‘a3’ from this study, at a projected distance of $R = 31$ kpc slightly off the minor axis, and RG02’s 19 kpc minor-axis field—and both studies are hampered by small number statistics. Future papers from our survey will use all of the existing fields with DEIMOS spectra (about half a dozen locations scattered around M31) and it should be possible to derive tighter constraints on the dynamics of the halo.

5. Chemical Abundance (and Age)

The giant southern stream in M31 appears to be the remnant of a massive/luminous satellite. The chemical abundance and age distribution of the stream are best viewed in the context of the ensemble of former satellites that merged to form the galaxy’s halo. With this goal in mind, we compare the properties of luminous RGB stars in the stream and to those in the general halo. The analysis of RGB star metallicities in this section is based mostly on their photometric properties with limited use of spectroscopic information; a full analysis of spectroscopic chemical abundances will be presented in a future paper. Some indirect age constraints are also obtained in this section.

5.1. Photometric Metallicity Estimates

5.1.1. Measurement Method and Errors

Photometric metallicity estimates are obtained for the 68 confirmed M31 RGB stars in our field ‘a3’ sample. As illustrated in Figure 2(d), the position of each star in the I_0 versus $(V -$

I_0 CMD is compared to a set of model RGB fiducials (Girardi et al. 2000). The conversion of stellar photometry from the Washington system to the Johnson/Cousins system and star-by-star dereddening are described in § 2.1. The fiducials span a wide range of metallicities for an age of $t = 12.6$ Gyr; they have been placed on the CMD using a true distance modulus of $(m-M)_0 = 24.47$ corresponding to an adopted distance to M31 of 783 kpc (Stanek & Garnavich 1998; Holland 1998). In order to estimate $[\text{Fe}/\text{H}]_{\text{phot}}$ for the stars, a Legendre polynomial of 6th order in $(V - I)_0$ and 10th order in I_0 is used to interpolate between the model RGB tracks.

If an M31 star is 2–6 Gyr old instead of our assumed age of 12.6 Gyr, its photometric metallicity estimate would need to be revised upwards by about +0.3 dex [e.g., a $t = 6.3$ Gyr fiducial is shown as a dashed line in Fig. 2(a)]. The overall uncertainty in the metallicities is about 0.3 dex, dominated by systematic errors such as age error/spread, residual differential reddening, $[\alpha/\text{Fe}]$ variations, and model inaccuracies; however, relative metallicity rankings can be achieved to somewhat greater accuracy than this for stars of comparable age. For stars located above the RGB tip in the CMD, the $[\text{Fe}/\text{H}]_{\text{phot}}$ estimates are based on linear extrapolation and are therefore very uncertain.

5.1.2. Selection Biases

Before studying the metallicity distribution of M31 stars, we investigate whether our RGB star sample is an unbiased sample. A couple of selection effects in particular are worth discussing.

It is well known that metal-line blanketing causes the RGB tip gets fainter with increasing metallicity. This causes the most metal-rich of the luminous RGB stars, those with $[\text{Fe}/\text{H}] \gtrsim -1$, to be underrepresented in any magnitude-limited sample. RG02 characterized this bias in detail and corrected for it. We do not correct for the bias in this paper since we are primarily interested in a differential stream versus general halo comparison rather than the absolute shape of the $[\text{Fe}/\text{H}]$ distribution. Moreover, the bias should be less pronounced in our field ‘a3’ sample (and the rest of the DEIMOS survey) than in RG02’s sample: they used a limiting I -band magnitude of 22.0, whereas our study used 22.0 for list 1 primary targets but relaxed it to 22.5 for lists 2–4 secondary and “filler” targets (§ 2.1.2).

Since metallicity is the second parameter (after surface gravity) in determining the strength of the Mg b/MgH feature, our *DDO51*-based spectroscopic target selection procedure is expected to introduce a bias against the most metal-rich RGB stars (§ 2.1.1). We investigate this by plotting $[\text{Fe}/\text{H}]_{\text{phot}}$ versus P_{giant} in Figure 9. There is no strong or obvious trend for the primary and secondary spectroscopic targets ($P_{\text{giant}} > 0.5$) that form the bulk of the sample. The handful of lists 3–4 “filler” targets in our sample with $P_{\text{giant}} < 0.5$ appear to have the same $[\text{Fe}/\text{H}]_{\text{phot}}$ distribution as the rest of the sample—they are *not* particularly metal rich. This test will ultimately be carried out with a larger sample of “filler” targets from the full DEIMOS survey. In summary, it appears that *DDO51*-based pre-screening does not introduce any strong metallicity bias over that introduced by I -band selection.

5.1.3. Comparing Metallicity Distributions

The metallicity distribution of RGB stars in M31’s giant southern stream is compared to that of its general halo in Figure 10. The top panel shows radial velocity as a function of metallicity for 68 confirmed RGB stars. The portion below the dashed horizontal line is the velocity range occupied by the stream, $v < -410 \text{ km s}^{-1}$. It appears that the 47 stars in this range are more skewed towards high metallicities than the 21 stars outside it. The thin solid histogram in the lower panel is the $[\text{Fe}/\text{H}]_{\text{phot}}$ distribution of stars in the stream’s velocity range, while the dashed histogram represents the non-stream general halo population. We will show below that the stream contains a few stars brighter than the RGB tip; $[\text{Fe}/\text{H}]_{\text{phot}}$ estimates for such stars are unreliable because they are based on a naive linear upward extrapolation of the RGB fiducials (§ 5.1.1). We therefore recompute the stream’s metallicity distribution, this time excluding the seven stars that lie above the tips of the model RGB tracks (bold solid histogram).

The stream appears to be more metal-rich on average than the general halo, $\langle [\text{Fe}/\text{H}] \rangle = -0.51$ versus -0.74 , and appears to have a smaller metallicity spread, 0.25 versus 0.40 dex. A two-sided Kolmogorov-Smirnov test indicates that there is only a 5% probability that the two $[\text{Fe}/\text{H}]$ distributions are drawn from the same parent distribution—in other words, the apparent difference between the stream and general halo metallicity distributions is a 2σ effect. Another difference between stream and general halo populations is evident from the CMD [Fig. 2(*d*)]: There are nine M31 stars that lie near or above the RGB tip and all nine are in the stream’s radial velocity range (pentagons). A couple of these stars in particular are more than 0.5 mag above M31’s RGB tip and yet must be M31 members given their large negative radial velocities. These are best explained in terms of an intermediate-age asymptotic giant branch (AGB) population in the stream.

Two pieces of information suggest that the *true* mean metallicity of the stream may be even higher, and the difference in mean metallicity between the stream and general halo larger/more significant, than observed. First, if a sizeable fraction of the RGB stars in the stream are indeed of intermediate age, then their photometric $[\text{Fe}/\text{H}]$ estimates will need to be corrected upward by about +0.3 dex. Second, any bias resulting from our photometric selection procedure will tend to deplete/truncate the high end of the $[\text{Fe}/\text{H}]$ distribution (§ 5.1.2), the end where the difference between the stream and general halo distributions appears to be the greatest.

Even if the observed mean metallicity of the stream is taken at face value, it points to a relatively high luminosity for the progenitor satellite galaxy of the stream. An empirical correlation between metallicity and luminosity has been noted for dwarf satellite galaxies in the Local Group (Mateo 1998; Grebel & Guhathakurta 1999; Dekel & Woo 2003) which would indicate an absolute *B*-band magnitude of $M_B \sim -17$ for the stream’s progenitor, or a luminosity of $L_B \approx 10^9 L_\odot$. This is consistent with the lower limits on progenitor luminosity derived from the stream’s width and internal velocity dispersion in Paper II.

The mean $[\text{Fe}/\text{H}]$ of -0.7 dex observed for the general halo population in field ‘a3’, and its total range of 1.5 dex, are broadly consistent with published studies of the metallicity distribution

in other fields around the M31 halo (Mould & Kristian 1986; Durrell, Harris, & Pritchett 1994, 2001, 2004; Rich et al. 1996; Holland, Fahlman, & Richer 1996; Reitzel, Guhathakurta, & Gould 1998; Sarajedini & van Duyne 2001; Bellazzini et al. 2003). However several factors make it difficult for us to carry out detailed comparisons or to draw firm conclusions about real metallicity variations from field to field. First, our field ‘a3’ general halo $[\text{Fe}/\text{H}]$ distribution is based on only 21 RGB stars and therefore suffers from large Poisson fluctuations. Second, while our study like these others is based on photometry of RGB stars, there are significant differences in terms of data analysis techniques and associated systematic errors, sample definition, contamination issues, and selection biases. The RG02 study may be comparable to ours since both are based on spectroscopy of RGB stars. We note that RG02 found the halo to be significantly more metal poor, by $\gtrsim 0.5$ dex in the mean, with a tail in the $[\text{Fe}/\text{H}]$ distribution extending down to $\lesssim -2$ dex that is simply not seen in the present study [see their Fig. 17(c)]. This may be yet another sign of substructure in M31’s halo, something that needs to be confirmed using larger, more uniformly selected, and directly comparable samples.

5.2. Spectroscopic Constraints on Metallicity

The discussion of the chemical abundance distribution in M31’s halo has so far been based purely on photometric metallicity estimates. In this section we present a brief analysis of the Ca II line strength in the spectra of RGB stars. The EW(Ca) measurement has a relatively large uncertainty associated with it, compared to the random error in $[\text{Fe}/\text{H}]_{\text{phot}}$ say, so we prefer not to translate it into an estimate of the spectroscopic metallicity $[\text{Fe}/\text{H}]_{\text{spec}}$. Instead the Ca II line strength is used as a point of comparison between photometric and spectroscopic metallicity estimates. We demonstrate that the two are in good agreement.

5.2.1. Predicted Calcium Line Strength

The photometric properties of each star are used to predict the strength of its Ca II triplet. First, the photometric metallicity estimate $[\text{Fe}/\text{H}]_{\text{phot}}$ (§ 5.1.1) is taken to be the same as the metallicity on the spectroscopic scale defined by Carretta & Gratton (1997), $[\text{Fe}/\text{H}]_{\text{CG97}}$. Next, we use a well-established empirical calibration relation, based on luminous RGB stars in Milky Way globular clusters, to derive $[\text{Fe}/\text{H}]_{\text{CG97}}$ from the Ca II triplet (Rutledge, Hesser, & Stetson 1997a; Rutledge et al. 1997b):

$$[\text{Fe}/\text{H}]_{\text{CG97}} = -2.66 + 0.42 [\Sigma\text{Ca} - 0.64(V_{\text{HB}} - V)] \quad (2)$$

where ΣCa is the weighted sum of the EWs, in units of Å, of the three lines comprising the Ca II triplet:

$$\Sigma\text{Ca} \equiv 0.5 \text{EW}(\lambda 8498 \text{Å}) + 1.0 \text{EW}(\lambda 8542 \text{Å}) + 0.6 \text{EW}(\lambda 8662 \text{Å}) \quad (3)$$

and the luminosity-based correction for the effect of surface gravity is made relative to the apparent magnitude of M31’s horizontal branch: $V_{\text{HB}} = 25.17$ (Holland et al. 1996). Inverting equation (2),

the *predicted* Ca II line strength is defined to be:

$$\Sigma\text{Ca}_{\text{pred}} \equiv 6.33 + 2.38 [\text{Fe}/\text{H}]_{\text{phot}} + 0.64(V_{\text{HB}} - V) \quad (4)$$

Since this relation is based on Galactic globular cluster RGB stars, we are making the implicit assumption that M31 RGB stars are comparably old ($t \gtrsim 10$ Gyr) and, more importantly, alpha-enhanced to the same degree ($[\alpha/\text{Fe}] = +0.3$ dex). As discussed in § 5.2.2 below, RGB stars are grouped according to the $\Sigma\text{Ca}_{\text{pred}}$ parameter for the purpose of coadding spectra.

5.2.2. *Stellar Absorption Features and Coadded Spectra*

The normalized 1D spectra shown in Figure 3 are arranged in order of the stars’ $(V - I)_0$ color becoming redder upwards. The onset of the TiO band seems to occur at $(V - I)_0 \sim 1.8$ which corresponds to $T_{\text{eff}} = 4000$ K (Alonso et al. 1999). As might be expected, there is a good correlation between the observed broad-band color and the strength of the TiO bands for stars that are redder (cooler) than this. Other features, such as the Ca II triplet and occasionally the Na I doublet, are also visible. It should be noted however that the 1D spectra shown in Figure 3 represent the best third of our sample. Unfortunately the spectral S/N ratio is not high enough to support a detailed star-by-star abundance analysis of all RGB stars in our sample.

We have decided therefore to coadd the 92 spectra (including 8 duplicate observations) in groups of about a dozen to improve the S/N. The spectra are grouped according to the expected Ca II triplet absorption line strengths of the stars, $\Sigma\text{Ca}_{\text{pred}}$. Two different grouping schemes are tried. In the first scheme, no distinction is made between stream versus general halo populations and the entire set of RGB stars are simply divided into five bins by line strength. In the second scheme, the 47 RGB stars in the stream’s radial velocity range are divided into four bins and the 21 general halo RGB stars outside this range into two bins. In both schemes, the 16 Galactic dwarf stars are placed in a bin by themselves. All spectra are shifted to zero velocity (rest frame) and then combined with inverse-variance weighting. The resulting coadded spectra are then smoothed with a weighted boxcar of width 5 pixels (1.7\AA), comparable to the instrumental resolution.

Figure 11 shows the six coadded spectra using the first grouping scheme. The lowest coadded spectrum is that of Milky Way dwarfs and the next five are M31 RGB star coadded spectra with predicted line strength increasing upwards. The top spectrum (bold line) is a model RGB spectrum from Schiavon & Barbuy (1999) computed using $T_{\text{eff}} = 4000$ K, $\log(g) = 1.5$, and $[\text{Fe}/\text{H}] = -0.3$. It is merely used to illustrate/identify usable absorption features in the far red region of the spectrum—e.g., Ca, Fe, Mg, Ti, and V lines for RGB stars, and these plus the surface-gravity-sensitive Na I doublet for dwarfs. A detailed quantitative treatment of absorption lines is postponed until a future paper; only the Ca II line strengths are discussed briefly below. We have therefore not made any attempt to fine tune the match between model and data in terms of line strength or spectral resolution.

5.2.3. Measured Calcium Line Strength and Some Sanity Checks

The EWs of the Ca II lines are measured in all coadded spectra using an 18\AA -window for each line. The continuum level (close to unity, since these are normalized spectra) is measured on either side of each Ca II line using windows of the same width while avoiding regions of the spectrum known to contain other strong lines (see RGB model spectrum in Fig. 11). For each spectrum the weighted sum of the EWs of the three Ca II lines, $\Sigma\text{Ca}_{\text{meas}}$, is computed according to equation (3).

Figure 12 compares the measured versus predicted combined Ca II EWs for the seven coadded spectra from the second grouping scheme defined above. It is reassuring to see that the M31 RGB coadds, both stream and general halo stars (pentagons and squares, respectively), lie close to the one-to-one line. There is a slight mismatch for the most strong-lined (metal-rich) stream RGB stars. If these happen to be intermediate-age stars—i.e., in the $\approx 2\text{--}6$ Gyr range instead of the 12.6 Gyr age that is assumed in fitting model RGB fiducials—their photometric metallicity estimates would be biased low by -0.3 dex (§ 5.1.1). Thus the $\Sigma\text{Ca}_{\text{pred}}$ values would be biased low by 0.7\AA (eq. [4]) and would, for the most part, explain the observed offset from the one-to-one line. This assumes that intermediate-age RGB stars follow the same $\Sigma\text{Ca} \rightarrow [\text{Fe}/\text{H}]_{\text{CG97}}$ calibration relation as old RGB stars (eq. [2]), which is yet to be verified.

Eight of the nine potential intermediate-age AGB stars (near/above the RGB tip in the CMD) are in the first bin for spectral coadds of stream stars in Figure 12—i.e., they have among the lowest $\Sigma\text{Ca}_{\text{pred}}$ values and are expected to have relatively weak Ca II lines. This bin also contains 4 normal metal-poor RGB stars located well below the RGB tip. The coadded spectrum for this group of stars appears to have a “normal” Ca II triplet strength, in that it lies close to the $\Sigma\text{Ca}_{\text{meas}} = \Sigma\text{Ca}_{\text{pred}}$ line, but it is not clear how to interpret this. If the stars above/near the RGB tip are indeed intermediate-age AGB stars: (i) $[\text{Fe}/\text{H}]_{\text{phot}}$ estimates are bound to be inaccurate as they are based on an arbitrary extrapolation of the RGB fiducials (§ 5.1.1); and (ii) the empirical $\Sigma\text{Ca} \rightarrow [\text{Fe}/\text{H}]_{\text{CG97}}$ calibration relation (eq. [2]), which is based on RGB stars, is likely to be off for AGB stars. It is conceivable that these two errors are somehow cancelling each other out; a detailed investigation of these issues is beyond the scope of this paper.

Judging from their location on the CMD and the agreement between $\Sigma\text{Ca}_{\text{pred}}$ and $\Sigma\text{Ca}_{\text{meas}}$, it appears that about two-thirds of the stars in our M31 RGB sample are old: This includes the two bins containing general halo members and bins 2 and 3 from the stream population in Figure 12. If the nine stream stars located above the RGB tip in the CMD (most are in stream bin 1) and the dozen strong-lined stream RGB stars located above/to the left of the $\Sigma\text{Ca}_{\text{meas}} = \Sigma\text{Ca}_{\text{pred}}$ line (stream bin 4) all turn out to have ages $t \lesssim 8$ Gyr as suspected, it would imply that about 30% of the overall M31 RGB population in field ‘a3’ is of intermediate age.

In a recent deep *Hubble Space Telescope* study of M31 main-sequence turnoff stars in an inner halo field ($R = 7$ kpc), Brown et al. (2003) found a surprisingly high fraction of intermediate-age stars, $\approx 30\%$. It has been suggested that the orbit of the giant southern stream might wrap around and intersect the Brown et al. field and that this might be responsible for the high intermediate-

age fraction seen there. If this explanation were correct, and taking our estimate of the field ‘a3’ intermediate-age fraction literally, the stream would stand out against the smooth halo population in the inner $R = 7$ kpc with the same 2:1 contrast as it does in our remote field ‘a3’. No such wrap-around portion of the stream is visible in the Ferguson et al. (2002) star-count map.

In contrast to the RGB stars, the foreground Galactic dwarf stars lie well below the $\Sigma\text{Ca}_{\text{meas}} = \Sigma\text{Ca}_{\text{pred}}$ line in Figure 12. The same effect was noted by RG02. This is yet another feature that can be used to distinguish between foreground dwarf star contaminants and M31 RGB stars (§ 3.3.5). It is evident from Figure 11 that the coadded dwarf star spectrum is significantly less noisy than the M31 RGB star coadds: This is because the former are $\Delta I \approx 1$ mag brighter on average [compare panels (c) and (d) of Fig. 2] and there are 16 stars in the former coadd versus 12 or 13 in the latter. The error in $\Sigma\text{Ca}_{\text{pred}}$ for the dwarfs is estimated to be 50% that of the M31 RGB stars. Thus, the offset of the dwarfs from the one-to-one line is highly significant.

6. Summary

The following are the main points of this paper:

- We are using the DEIMOS spectrograph on the Keck II 10-meter telescope to carry out a moderate-resolution ($R \lesssim 7000$) spectroscopic survey of a large sample of RGB stars in the outer halo of M31. This is the first paper from that survey and describes data from three DEIMOS slitmasks in field ‘a3’, located on the giant southern debris stream discovered by Ibata et al. (2001) at a projected distance of 31 kpc from the center of M31. The field ‘a3’ data presented here ($\gtrsim 200$ spectroscopic targets) represent about a quarter of the DEIMOS survey data obtained to date.
- Spectroscopic targets were selected using intermediate-band *DDO51* and Washington *M* and *T₂* photometry by discriminating between RGB stars and foreground Galactic dwarfs on the basis of surface gravity. The method has proved to increase the yield of bona fide M31 RGB stars in our sample.
- A sample of 68 definite M31 RGB stars is isolated. Careful attention is paid to the removal of sample contaminants, both background galaxies and especially foreground Milky Way dwarf stars. The latter are identified using a combination of data/methods: radial velocity, broad-band color-magnitude information, *DDO51* photometry, Ca II triplet line strength, and, most importantly, Na I doublet line strength.
- About two-thirds of the M31 RGB stars in our field appear to be members of its giant southern stream while the rest belong to the general halo population.
- The mean heliocentric radial velocity of the stream in field ‘a3’ is -458 km s^{-1} which translates to -158 km s^{-1} with respect to the systemic velocity of M31. The stream has a relatively

low internal line-of-sight velocity dispersion: 15^{+8}_{-15} km s⁻¹ (90% confidence limits from a maximum likelihood analysis). The interpretation of these and other data on the kinematics and three-dimensional structure of the stream, in the context of possible orbits and progenitor properties, is presented in the companion paper by Font et al. (2004, Paper II).

- The rms metallicity spread of M31’s giant southern stream is 0.25 dex and its mean metallicity is $\langle[\text{Fe}/\text{H}]\rangle = -0.51$, possibly higher if one corrects for selection bias against the highest metallicity RGB stars. This is indicative of a fairly luminous progenitor satellite galaxy. The photometric and spectroscopic metallicity estimates are in good agreement with each other for the majority of RGB stars in our sample.
- The most metal rich RGB stars in the stream have $[\text{Fe}/\text{H}]_{\text{spec}} > [\text{Fe}/\text{H}]_{\text{phot}}$ (anomalously strong Ca II lines). The stream also contains a few stars that lie above the RGB tip in the CMD. Both findings suggest that the stream contains a non-negligible fraction of intermediate-age stars.
- The general halo population in field ‘a3’ has a mean metallicity of $\langle[\text{Fe}/\text{H}]\rangle = -0.74$ and thus appears to be more metal poor than the stream on average. The halo component has a broad metallicity distribution spanning about 1.5 dex.
- There is a hint of halo substructure in M31 based on the radial velocity (and possibly metallicity) distribution of the general halo RGB population in this field.

We are grateful to Sandy Faber and the DEIMOS team for building an outstanding instrument and for extensive help and guidance during its first observing season. We also thank Alison Coil, Drew Phillips, and Greg Wirth for observing field ‘a3’ masks #2 and #3 on our behalf, Drew Phillips for help with slitmask designs, Ricardo Schiavon for providing a model RGB spectrum and expert advice on spectral features, Jeff Lewis and Matt Radovan in the Lick instrument shops for their careful and timely fabrication of the masks, and the DEEP2 team for allowing us use of the `spec1d/zspec` software. The `spec2d` data reduction pipeline for DEIMOS was developed at UC Berkeley with support from NSF grant AST-0071048. P.G. acknowledges support from NSF grant AST-0307966 and a Special Research Grant from UCSC. R.M.R. and D.B.R.’s contributions were supported by NSF grant AST-0307931. S.R.M., J.C.O., and R.J.P. acknowledge funding by NSF grants AST-0307842 and AST-0307851, NASA/JPL contract 1228235, the David and Lucile Packard Foundation, and The F. H. Levinson Fund of the Peninsula Community Foundation. M.G. is supported by NASA through Hubble Fellowship grant HF-01159.01-A awarded by the Space Telescope Science Institute, which is operated by the Association of Universities for Research in Astronomy, Inc., under NASA contract NAS 5-26555. K.V.J.’s contribution was supported through NASA grant NAG5-9064 and NSF CAREER award AST-0133617.

REFERENCES

- Alonso, A., Arribas, S., & Martínez-Roger, C. 1999, *A&AS*, 140, 261
- Bahcall, J. N., & Soneira, R. M. 1984, *ApJS*, 55, 67
- Bellazzini, M., Cacciari, C., Federici, L., Fusi Pecci, F., & Rich, R. M. 2003, *A&A*, 405, 867
- Binney, J., & Tremaine, S. 1987, *Galactic Dynamics*, Princeton University Press, Princeton
- Brown, T. M., Ferguson, H. C., Smith, E., Kimble, R. A., Sweigart, A. V., Renzini, A., Rich, R. M., & VandenBerg, D. A. 2003, *ApJ*, 592, L17
- Bullock, J. S., Kravtsov, A. V., & Weinberg, D. H. 2001, *ApJ*, 548, 33
- Cardelli, J. A., Clayton, G. C., & Mathis, J. S. 1989, *ApJ*, 345, 245
- Carretta, E., & Gratton, R. G. 1997, *A&AS*, 121, 95
- Choi, P. I., Guhathakurta, P., & Johnston, K. V. 2002, *AJ*, 124, 310
- Coil, A. L., et al. 2004, *ApJ*, in press (astro-ph/0305586)
- Crane, J. D., Majewski, S. R., Rocha-Pinto, H. J., Frinchaboy, P. M., Skrutskie, M. F., & Law, D. R. 2003, *ApJ*, 594, L119
- Dekel, A. & Woo, J. 2003, *MNRAS*, 344, 1131
- Durrell, P. R., Harris, W. E., & Pritchett, C. J. 1994, *AJ*, 108, 2114
- Durrell, P. R., Harris, W. E., & Pritchett, C. J. 2001, *AJ*, 121, 2557
- Durrell, P. R., Harris, W. E., & Pritchett, C. J. 2004, *AJ*, in press (astro-ph/0405403)
- Evans, N. W., & Wilkinson, M. I. 2000, *MNRAS*, 316, 929
- Faber, S. M., et al. 2003, *Proc. SPIE*, 4841, 1657
- Ferguson, A. M. N., Irwin, M. J., Ibata, R. A., Lewis, G. F., & Tanvir, N. R. 2002, *AJ*, 124, 1452
- Font, A., Johnston, K. V., Guhathakurta, P., Majewski, S. R., & Rich, R. M. 2004, *AJ*, submitted (Paper II)
- Girardi, L., Bressan, A., Bertelli, G., & Chiosi, C. 2000, *A&AS*, 141, 371
- Grebel, E. K., & Guhathakurta, P. 1999, *ApJ*, 511, L101
- Guhathakurta, P., & Reitzel, D. B. 2002, *BAAS*, 201, #14.11
- Helmi, A., & White, S. D. M. 1999, *MNRAS*, 307, 495

- Helmi, A., & de Zeeuw, T. 2000, MNRAS, 319, 657
- Holland, S. 1998, AJ, 115, 1916
- Holland, S., Fahlman, G. G., & Richer, H. B. 1996, AJ, 112, 1035
- Horne, K. 1986, PASP, 98, 609
- Ibata, R., Chapman, S., Ferguson, A. M. N., Irwin, M., Lewis, G., & McConnachie, A. 2004, MNRAS, in press (astro-ph/0403068)
- Ibata, R. A., Gilmore, G., & Irwin, M. J. 1994, Nature, 370, 194
- Ibata, R., Irwin, M. J., Ferguson, A. M. N., Lewis, G., & Tanvir, N. 2001, Nature, 412, 49
- Johnston, K. V. 1998, ApJ, 495, 297
- Johnston, K. V., Hernquist, L., & Bolte, M. 1996, ApJ, 465, 278
- Lewis, G. F., Ibata, R. A., Chapman, S. C., Ferguson, A. M. N., McConnachie, A. W., Irwin, M. J., & Tanvir, N. 2004, in 5th Galacto Chemodynamics conference, PASA, in press (astro-ph/0401092)
- Maddison, S. T., Kawata, D., & Gibson, B. K. 2002, Ap&SS, 281, 421
- Majewski, S. R. 1992, ApJS, 78, 87
- Majewski, S. R., Kunkel, W. E., Law, D. R., Patterson, R. J., Pollak, A. A., Rocha-Pinto, H. J., Crane, J. D., Frinchaboy, P. M., Hummels, C. B., Johnston, K. V., Rhee, J., Skrutskie, M. F., & Weinberg, M. 2004a, AJ, in press (astro-ph/0403701)
- Majewski, S. R., Munn, J. A., & Hawley, S. L. 1996, ApJ, 459, L73
- Majewski, S. R., Ostheimer, J. C., Kunkel, W. E., & Patterson, R. J. 2000, AJ, 120, 2550
- Majewski, S. R., Skrutskie, M. F., Weinberg, M. D., & Ostheimer, J. C. 2003, ApJ, 599, 1082
- Mateo, M. L. 1998, ARA&A, 36, 435
- Mathewson, D. S., Cleary, M. N., & Murray, J. D. 1974, ApJ, 190, 291
- McConnachie, A. W., Irwin, M. J., Ibata, R. A., Ferguson, A. M. N., Lewis, G. F., & Tanvir, N. 2003, MNRAS, 343, 1335
- McConnachie, A. W., Irwin, M. J., Lewis, G. F., Ibata, R. A., Chapman, S. C., Ferguson, A. M. N., & Tanvir, N. R. 2004, MNRAS, in press (astro-ph/0406055)
- Moore, B., & Davis, M. 1994, MNRAS, 270, 209

- Mould, J., & Kristian, J. 1986, *ApJ*, 305, 591
- Newberg, H. J., et al. 2003, *ApJ*, 596, L191
- Odenkirchen, M., et al. 2001, *ApJ*, 548, L165
- Oke, J. B., Cohen, J. G., Carr, M., Cromer, J., Dingizian, A., Harris, F. H., Labrecque, S., Lucinio, R., Schall, W., Epps, H., & Miller, J. 1995, *PASP*, 107, 375
- Ostheimer, J. C. 2002, Ph.D. thesis, University of Virginia
- Palma, C., Majewski, S. R., Siegel, M. H., Patterson, R. J., Ostheimer, J. C., & Link, R. 2003, *AJ*, 125, 1352
- Popowski, P., & Gould, A. 1998, *ApJ*, 506, 271
- Putman, M. E., Gibson, B. K., & Staveley-Smith, L. 1999, *ASP Conf. Ser.* 165: The Third Stromlo Symposium: The Galactic Halo, 113
- Ratnatunga, K. U., & Bahcall, J. N. 1985, *ApJS*, 59, 63
- Reitzel, D. B., & Guhathakurta, P. 2002, *AJ*, 124, 234 (RG02)
- Reitzel, D. B., Guhathakurta, P., & Gould, A. 1998, *AJ*, 116, 707
- Reitzel, D. B., Guhathakurta, P., & Rich, R. M. 2004, *AJ*, 127, 2133
- Rich, R. M., Mighell, K. J., Freedman, W. L., & Neill, J. D. 1996, *AJ*, 111, 768
- Rocha-Pinto, H. J., Majewski, S. R., Skrutskie, M. F., & Crane, J. D. 2003, *ApJ*, 594, L115
- Rockosi, C. M., et al. 2002, *AJ*, 124, 349
- Rutledge, G. A., Hesser, J. E., & Stetson, P. B. 1997a, *PASP*, 109, 907
- Rutledge, G. A., Hesser, J. E., Stetson, P. B., Mateo, M., Simard, L., Bolte, M., Friel, E., & Copin, Y. 1997b, *PASP*, 109, 883
- Sarajedini, A., & van Duyne, J. 2001, *AJ*, 122, 2444
- Schiavon, R. P., & Barbuy, B. 1999, *ApJ*, 510, 934
- Schiavon, R. P., Barbuy, B., Rossi, S. C. F., & Milone, A. 1997, *ApJ*, 479, 902
- Schlegel, D. J., Finkbeiner, D. P., & Davis, M. 1998, *ApJ*, 500, 525
- Searle, L., & Zinn, R. 1978, *ApJ*, 225, 357
- Spinrad, H., & Taylor, B. J. 1969, *ApJ*, 157, 1279

- Stanek, K. Z., & Garnavich, P. M. 1998, *ApJ*, 503, L131
- Stetson, P. B. 1992, in *Astronomical Data Analysis Software and Systems*, eds. D. M. Worrall, C. Biemesderfer, & J. Barnes, (ASP Conf. Ser., Vol. 25), 297
- Stetson, P. B. 1994, *PASP*, 106, 250
- Tonry, J., & Davis, M. 1979, *AJ*, 84, 1511
- White S. D. M., & Rees, M. J. 1978, *MNRAS*, 183, 341
- Yanny, B., et al. 2003, *ApJ*, 588, 824

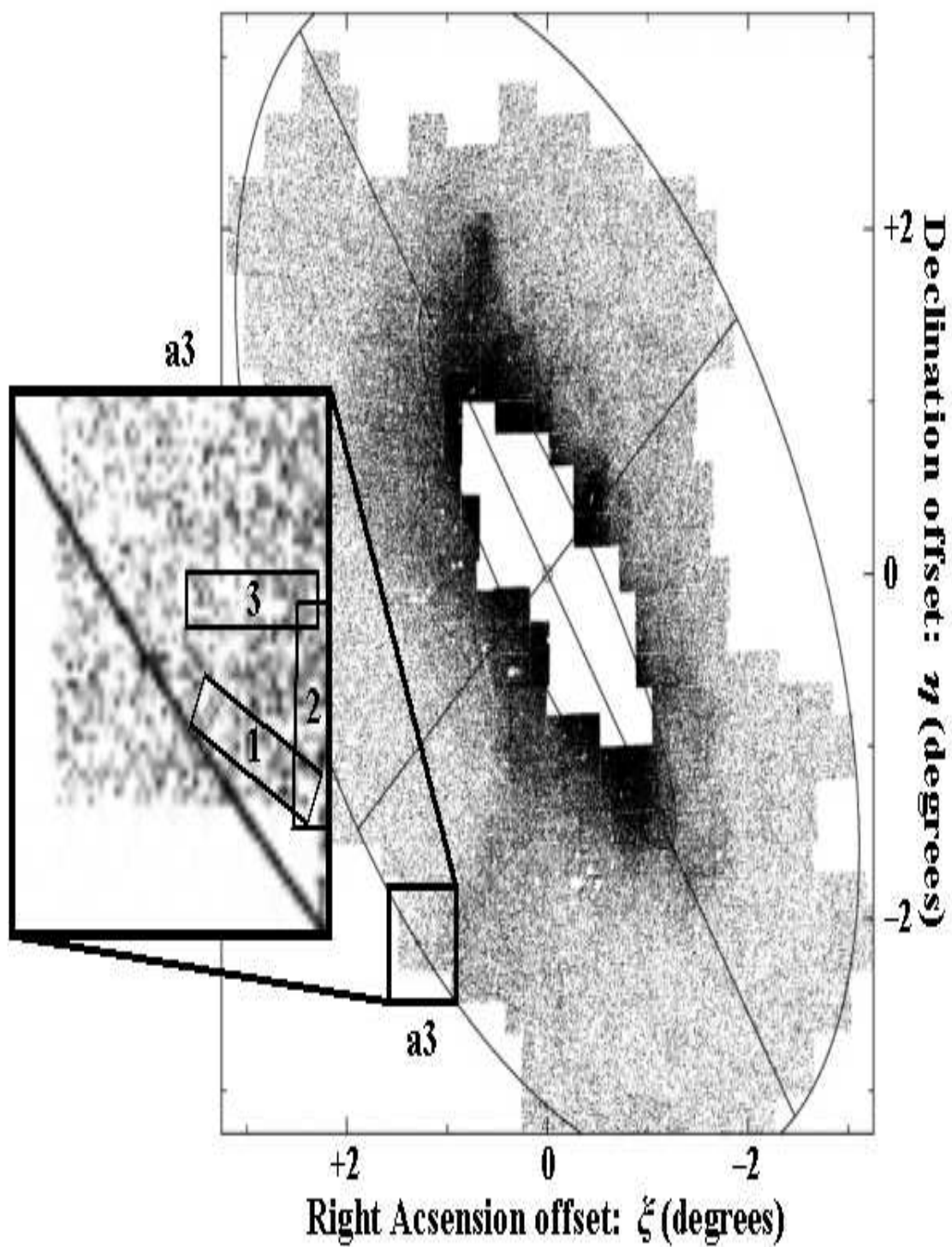


Fig. 1.— Sky position and orientation of the DEIMOS spectroscopic slitmasks (thin rectangles numbered 1–3 in the inset), against the star count map of metal-rich M31 RGB stars presented by

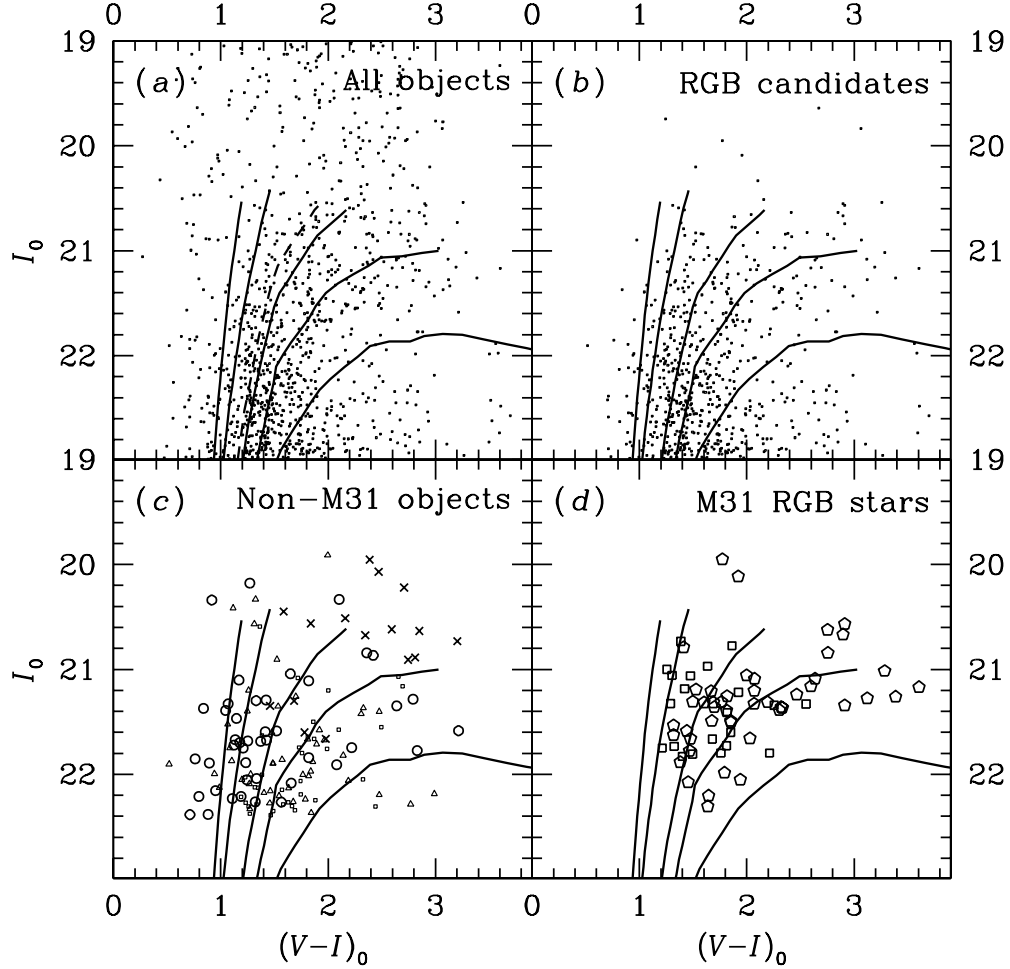


Fig. 2.— (a) Color-magnitude diagram of all objects in the portion of the ‘a3’ field covered by the three DEIMOS slitmasks. The Washington system M and T_2 photometry has been transformed to Johnson/Cousins V and I (Majewski et al. 2000) and corrected for foreground extinction/reddening (Schlegel et al. 1998). Red giant branch fiducials from the Padova group (Girardi et al. 2000) are shown for $t = 12.6$ Gyr and $[\text{Fe}/\text{H}] = -2.3, -1.3, -0.7, -0.4$, and 0.0 (solid lines, left→right) and $t = 6.3$ Gyr and $[\text{Fe}/\text{H}] = -0.7$ (dashed line). (b) Same as (a), except the $DDO51$ -based parameter $P_{\text{giant}} > 0.5$ is used to pre-select RGB candidates and the morphological selection criteria $\text{chi} < 1.3$ and $|\text{sharp}| < 0.3$ are used to reject background galaxies (§ 2.1). (c) Same as (a), for objects for which the radial velocity measurement fails because of low S/N (small squares) or lack of definite spectral features (small triangles), foreground Galactic dwarf stars (crosses), and background field galaxies (open circles); see § 2.4 for details. (d) Same as (a), for confirmed M31 RGB stars: potential members of the giant southern stream (open pentagons) and members of the general halo population (open squares). The M31 RGB stars are bracketed by model RGB tracks with a plausible range of metallicities, with the stream RGB stars being more metal rich on average than those in the general halo. Nine stars, all potential stream members, lie at or above the tip of the RGB tracks.

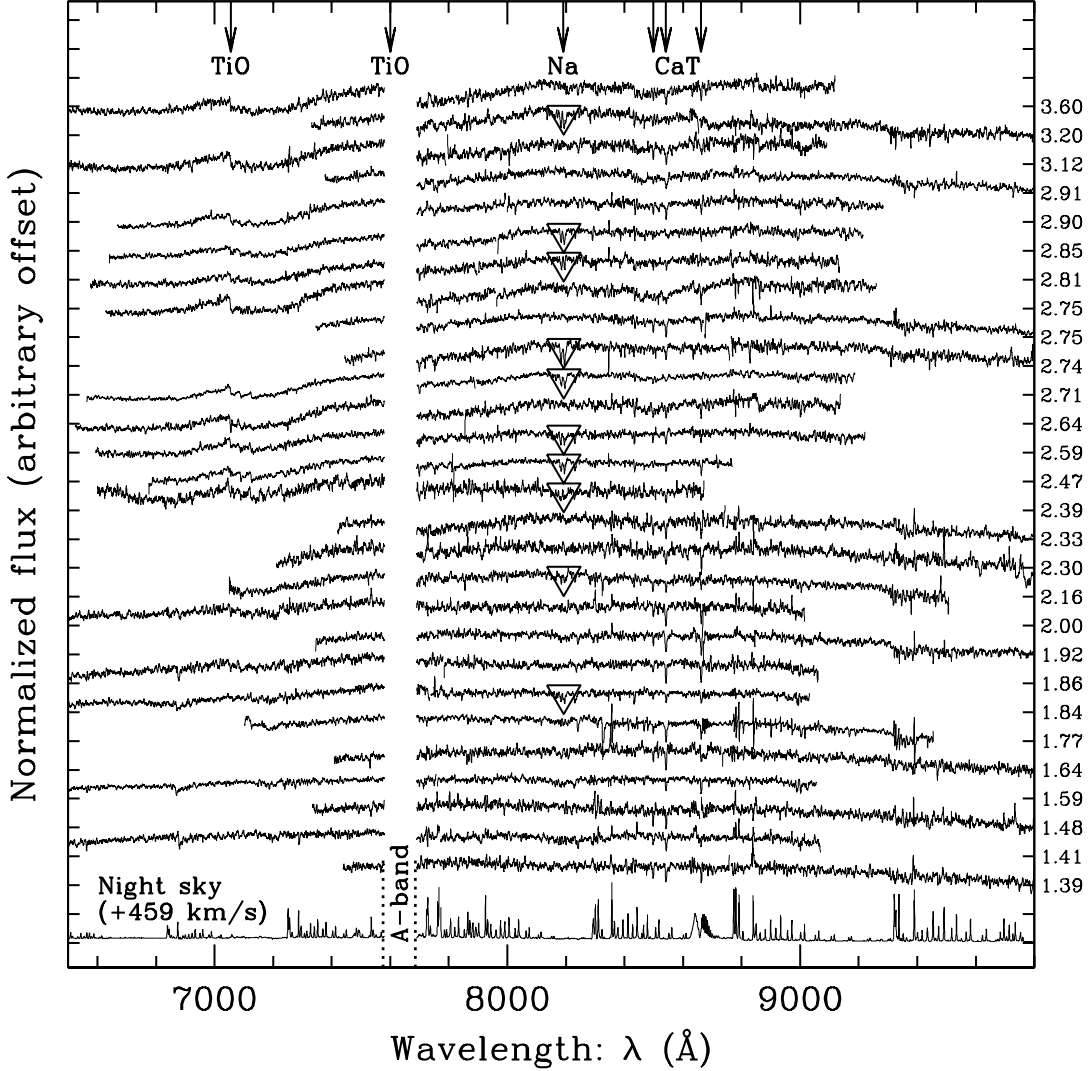


Fig. 3.— Montage of the best DEIMOS spectra ($S/N \gtrsim 12 \text{ Å}^{-1}$) of M31 RGB and Galactic dwarf stars. The spectra have been smoothed with a 3 Å weighted boxcar, shifted to zero velocity, normalized at $\sim 8500 \text{ Å}$, offset in y for illustration purposes (each tickmark represents unity), and ordered by $(V - I)_0$ color (indicated on the right side of the y axis). One of two instrument settings was used covering $\lambda\lambda 6500\text{--}9100 \text{ Å}$ or $\lambda\lambda 7200\text{--}9800 \text{ Å}$. The atmospheric A-band correction is inadequate in the present reduction so this region is excluded. The night sky spectrum (bottom), a composite from the two wavelength settings, has been smoothed and shifted by $+458 \text{ km s}^{-1}$, the mean shift for stars in M31’s giant southern stream. The strongest TiO bandheads, Na I doublet, and Ca II triplet lines are marked. The TiO bands increase in strength with $(V - I)_0$ color; the redder TiO band lies in the A-band gap but the break in the spectrum is apparent for red stars. The Na line is surface-gravity sensitive and thus a discriminator between M31 RGB stars and foreground Galactic dwarfs for $(V - I)_0 \gtrsim 2$ (latter marked by bold open triangles).

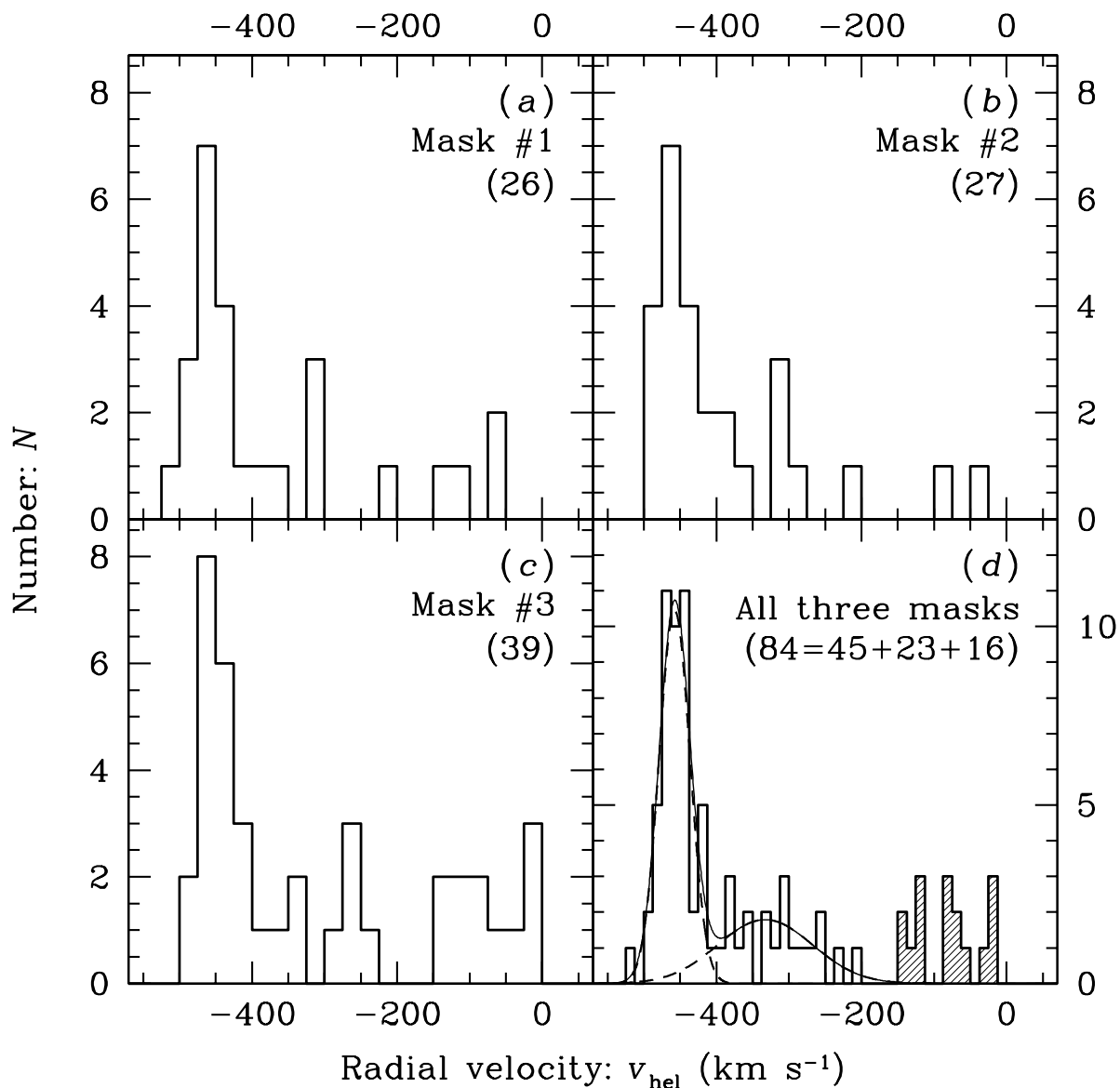


Fig. 4.— (a)–(c) Distribution of (heliocentric) radial velocities for stars on each of the three DEIMOS masks. The total number of objects in each histogram is indicated in parentheses. (d) Same as (a), for all three masks combined (note, 8 stars have duplicate measurements). The thin dashed lines show Gaussians representing M31 RGB stars in the giant southern stream (tall narrow peak) and general halo (short broad peak); the thin solid line is the sum of the two Gaussians (see Fig. 7 for the details of the maximum likelihood fit). The group of objects with $v > -150$ km s $^{-1}$ are candidate foreground Galactic dwarf stars (shaded histogram). The likely break up of the 84 stars is: 45 M31 stream RGB stars, 23 M31 halo RGB stars, and 16 foreground Galactic dwarfs (§§ 3.2–3.3).

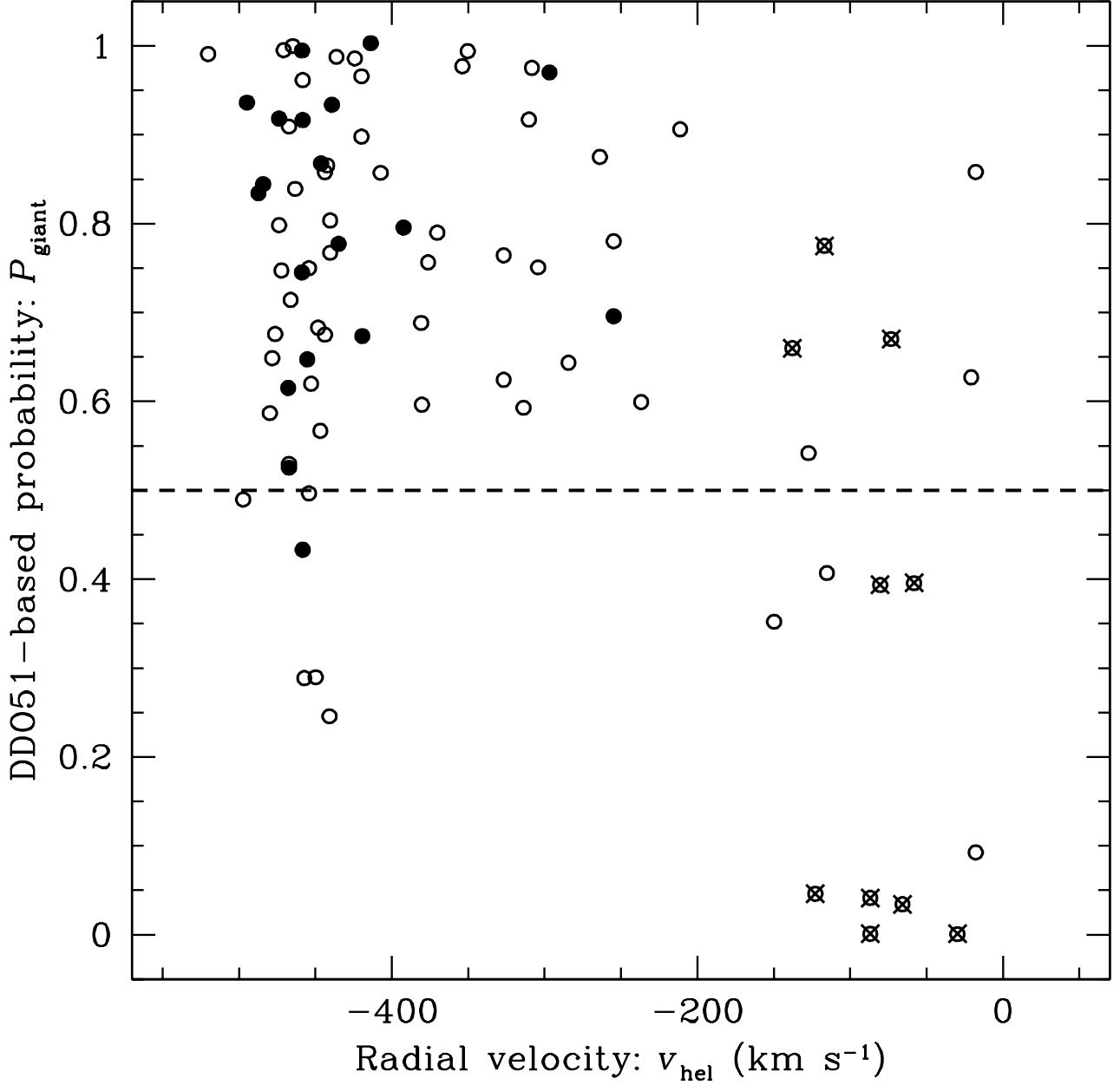


Fig. 5.— $DDO51$ -based probability of a star being a red giant plotted against radial velocity. Stars with $v > -150 \text{ km s}^{-1}$ are foreground Galactic dwarfs while the rest are M31 RGB stars. The dashed line separates primary/secondary spectroscopic targets with $P_{\text{giant}} > 0.5$ (lists 1 and 2) from “filler” targets with $P_{\text{giant}} < 0.5$ (lists 3 and 4; see § 2.1). For a subset of the stars (red stars with high S/N), the surface-gravity-sensitive $\lambda 8190\text{\AA}$ Na I doublet is used to make a definite classification of dwarfs (crosses) versus RGB stars (filled circles); see § 3.3.6 and Figure 6 for details. The P_{giant} values tend to be higher for confirmed RGB stars than dwarfs but it is not a perfect discriminator.

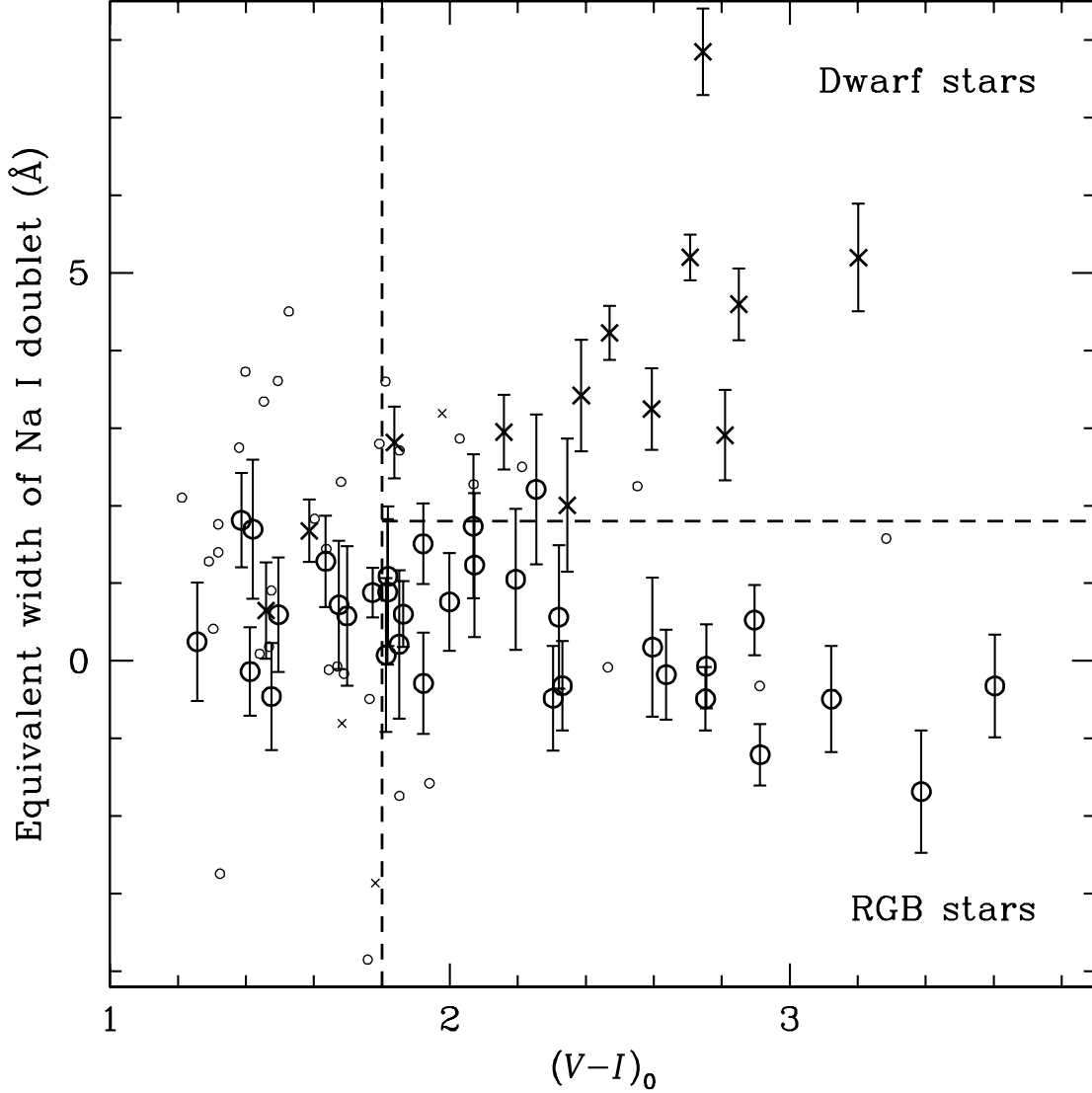


Fig. 6.— Equivalent width of the Na I doublet versus dereddened color for the 84 stars in our sample. The EW is calculated within a 21\AA -wide window. The uncertainty in line strength is estimated from stars with duplicate measurements under the assumption that it is inversely proportional to S/N; 1σ error bars are only shown when they are $< 1\text{\AA}$. The velocity-based subsamples of candidate M31 RGB stars and candidate Galactic dwarf stars are marked as crosses and circles, respectively. Cool stars [$T_{\text{eff}} < 4000$ K or $(V-I)_0 > 1.8$] have a bimodal distribution of Na I line strengths. The dashed lines are used to discriminate between RGB and dwarf stars—they are expected to occupy the bottom right and top right sections of the plot, respectively.

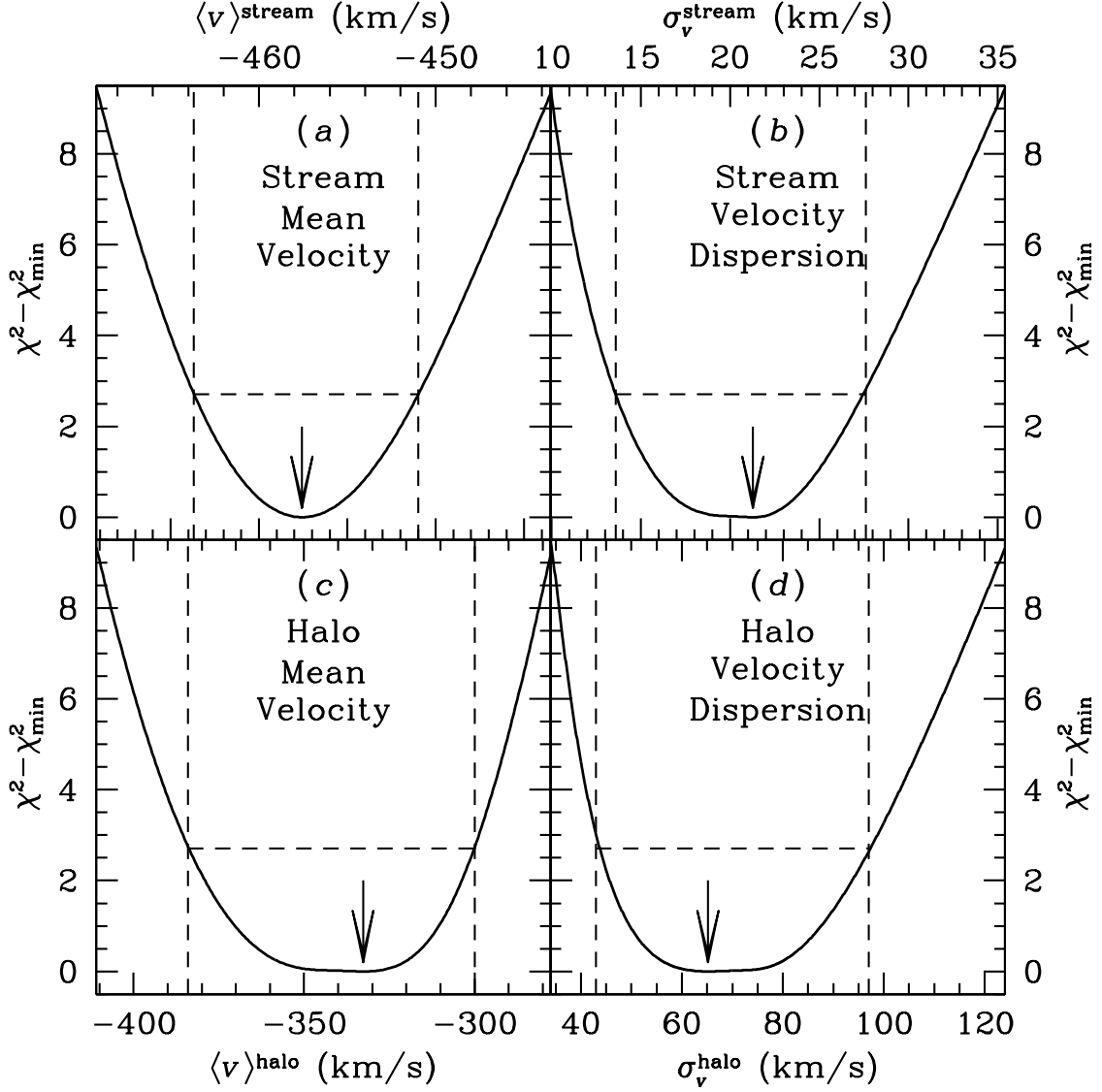


Fig. 7.— Results of a maximum likelihood fit of the sum of two Gaussians to the radial velocity distribution of M31 RGB stars. The difference between χ^2 and the minimum χ^2 is plotted as a function of (a) the mean velocity of the giant southern stream, (b) the stream velocity dispersion, (c) the mean velocity of the general halo population, and (d) the halo velocity dispersion. An arrow marks the best fit value and the dashed lines corresponds to the 90% confidence limits in each case.

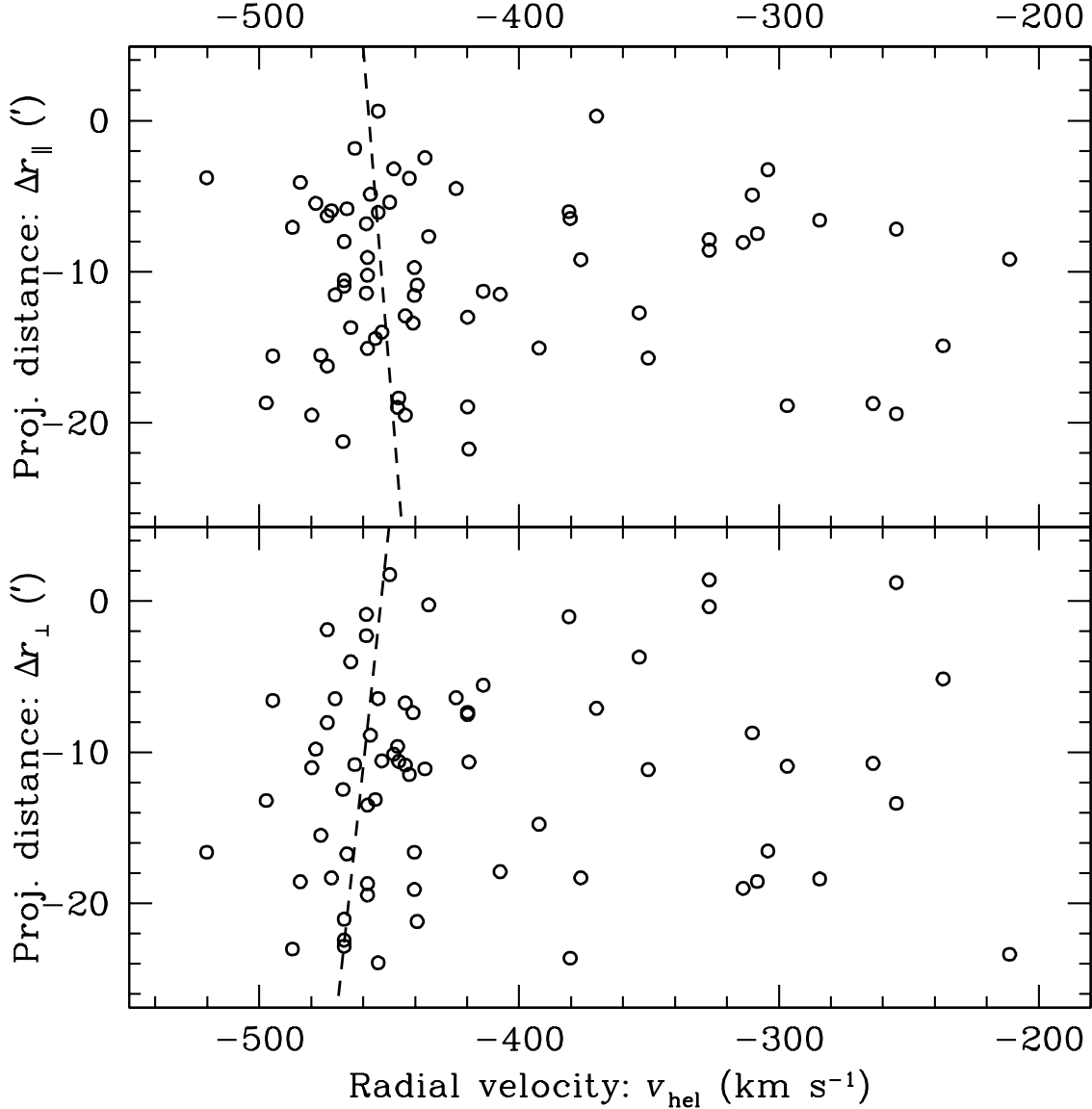


Fig. 8.— Projected position of M31 RGB stars along (*top*) and perpendicular to (*bottom*) the main length of the giant southern stream plotted against radial velocity. The stream is assumed to run northwest to southeast, and Δr_{\parallel} and Δr_{\perp} are measured relative to the center of the ‘a3’ field increasing towards the southeast and northeast, respectively (Fig. 1). The dashed lines indicate the gradients $\Delta v/\Delta r$ measured for candidate stream stars ($v < -410 \text{ km s}^{-1}$); the gradients are poorly determined because of uncertainty about which stars are members of the stream (as opposed to the general M31 halo) and because of the small number of stars. Our $\Delta v/\Delta r_{\parallel}$ measurement is consistent with that measured over a longer spatial baseline by Lewis et al. (2004) and Ibata et al. (2004); large values of $|\Delta v/\Delta r_{\perp}|$ are ruled out by the data.

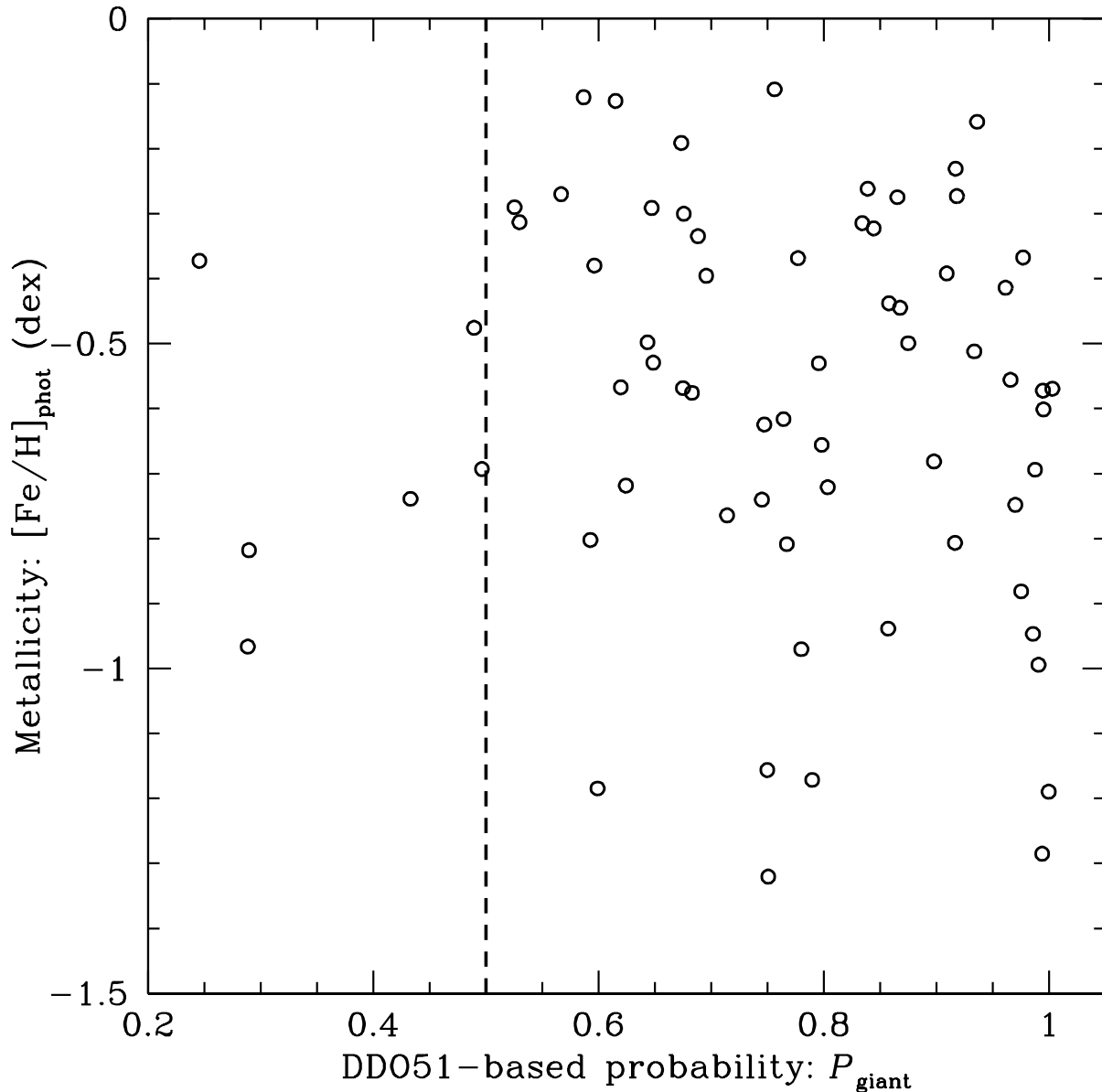


Fig. 9.— Photometric metallicity estimate versus P_{giant} , the *DDO*51-based probability of a star being a red giant. Only confirmed M31 RGB stars, those with $v < -200 \text{ km s}^{-1}$ are shown. Stars to the right of the dashed vertical line are primary and secondary RGB candidates (lists 1 and 2) while the ones to the left are “filler” targets (lists 3 and 4; see § 2.1.2). Two features of this plot suggest that *DDO*51-based pre-screening does *not* introduce any strong metallicity bias: (i) Stars with $P_{\text{giant}} > 0.5$ occupy a roughly rectangular region of the plot and show no obvious trend; and (ii) Even though there is only a handful of “filler” targets—i.e., those for which the *DDO*51 criterion was relaxed or dropped—they span the same range of $[\text{Fe}/\text{H}]_{\text{phot}}$ values as the rest of the stars.

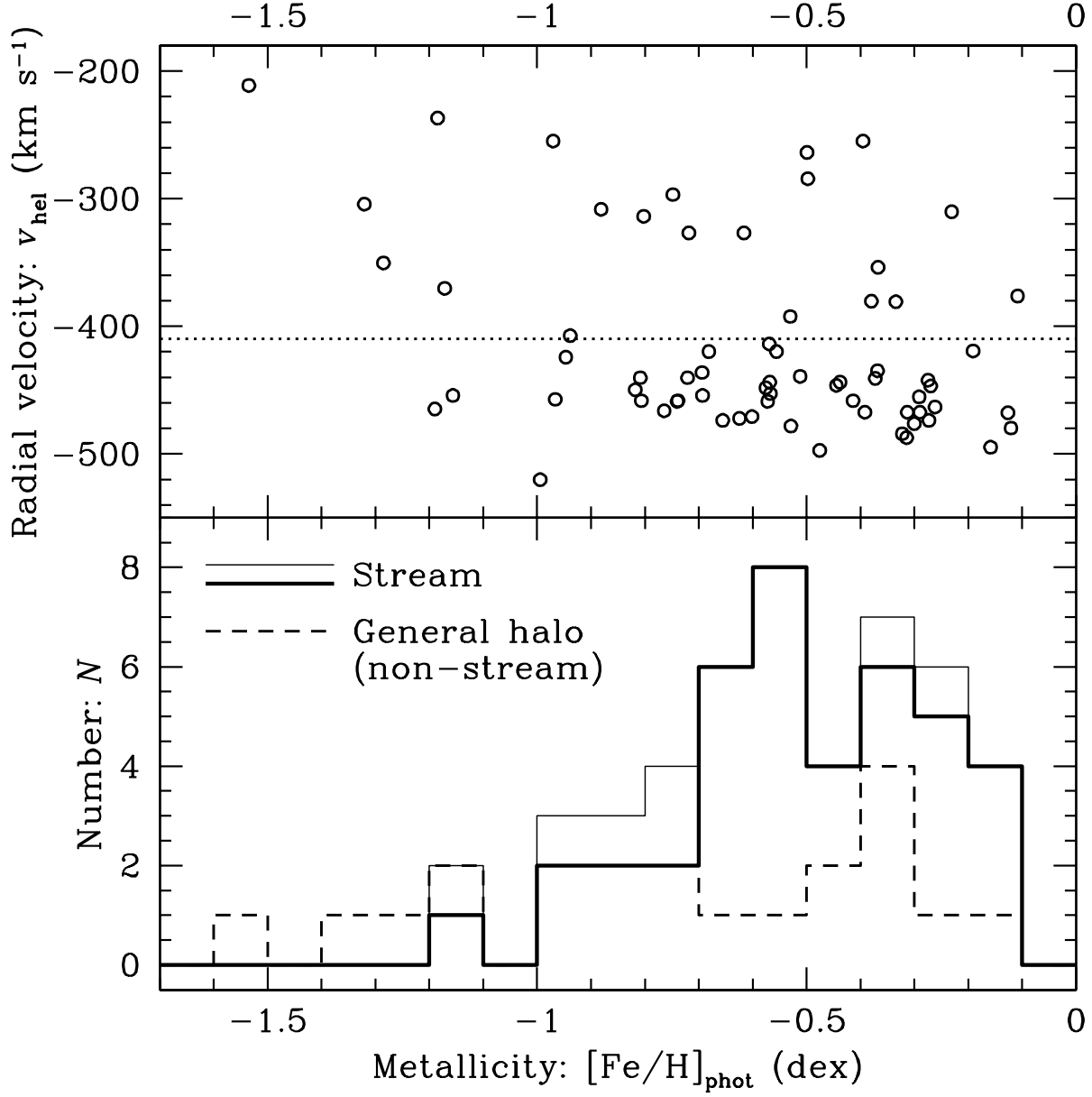


Fig. 10.— (Top) Radial velocity versus metallicity for M31 RGB stars, where the photometric metallicity estimate is derived by fitting model red giant tracks to the star in the color-magnitude diagram (Fig. 2). The velocity range below the dotted line is dominated by members of the giant southern stream. (Bottom) Metallicity distribution of M31 RGB stars in the stream’s velocity range, with and without the seven stars brighter than the RGB tip for which $[\text{Fe}/\text{H}]_{\text{phot}}$ estimates are unreliable (thin and bold solid histograms, respectively) and the non-stream general halo population (dashed histogram). We estimate that two of the 47 stars in the stream’s velocity range are actually members of the general halo population (§ 3.2). The stream appears to have a smaller metallicity spread than the general halo and a higher mean metallicity: $\langle [\text{Fe}/\text{H}]_{\text{phot}}(\text{stream}) \rangle \sim -0.51$ versus $\langle [\text{Fe}/\text{H}]_{\text{phot}}(\text{halo}) \rangle \lesssim -0.74$ (§ 5.1.3).

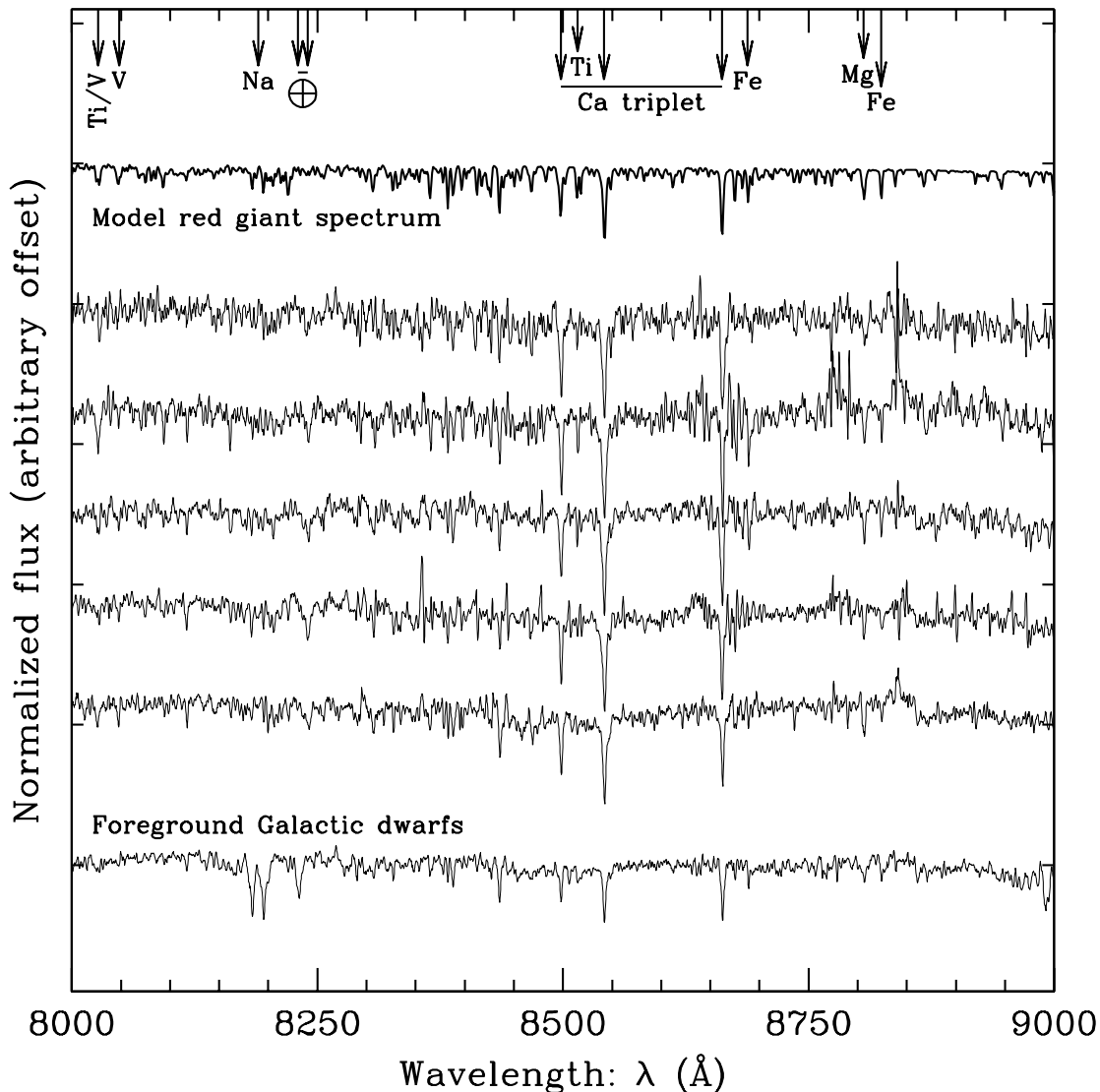


Fig. 11.— Montage of coadded DEIMOS spectra (thin solid lines) showing the region around the Ca II triplet, normalized and shifted to rest-frame wavelength and smoothed with a 1.7\AA weighted boxcar. The lowest spectrum is a coadd of 16 foreground Galactic dwarf stars. The next five spectra are coadds of about a dozen M31 RGB stars each, grouped and ordered by *predicted* Ca II line strength (increasing upward) as estimated from the CMD-based photometric metallicity and luminosity (§ 5.2.1). The bold line at the top is a model red giant spectrum with $T_{\text{eff}} = 4000\text{ K}$, $\log(g) = 1.5$, and $[\text{Fe}/\text{H}] = -0.3$ from Schiavon & Barbuy (1999). A few prominent spectral features of RGB stars are identified along with the $\lambda 8190\text{\AA}$ Na I doublet, which is strong in dwarfs. Because we have corrected the M31 RGB and Galactic dwarf spectra to zero velocity, the $\lambda 8228\text{\AA}$ telluric feature is Doppler shifted to $\sim \lambda 8231\text{\AA}$ and $\sim \lambda 8240\text{\AA}$, respectively.

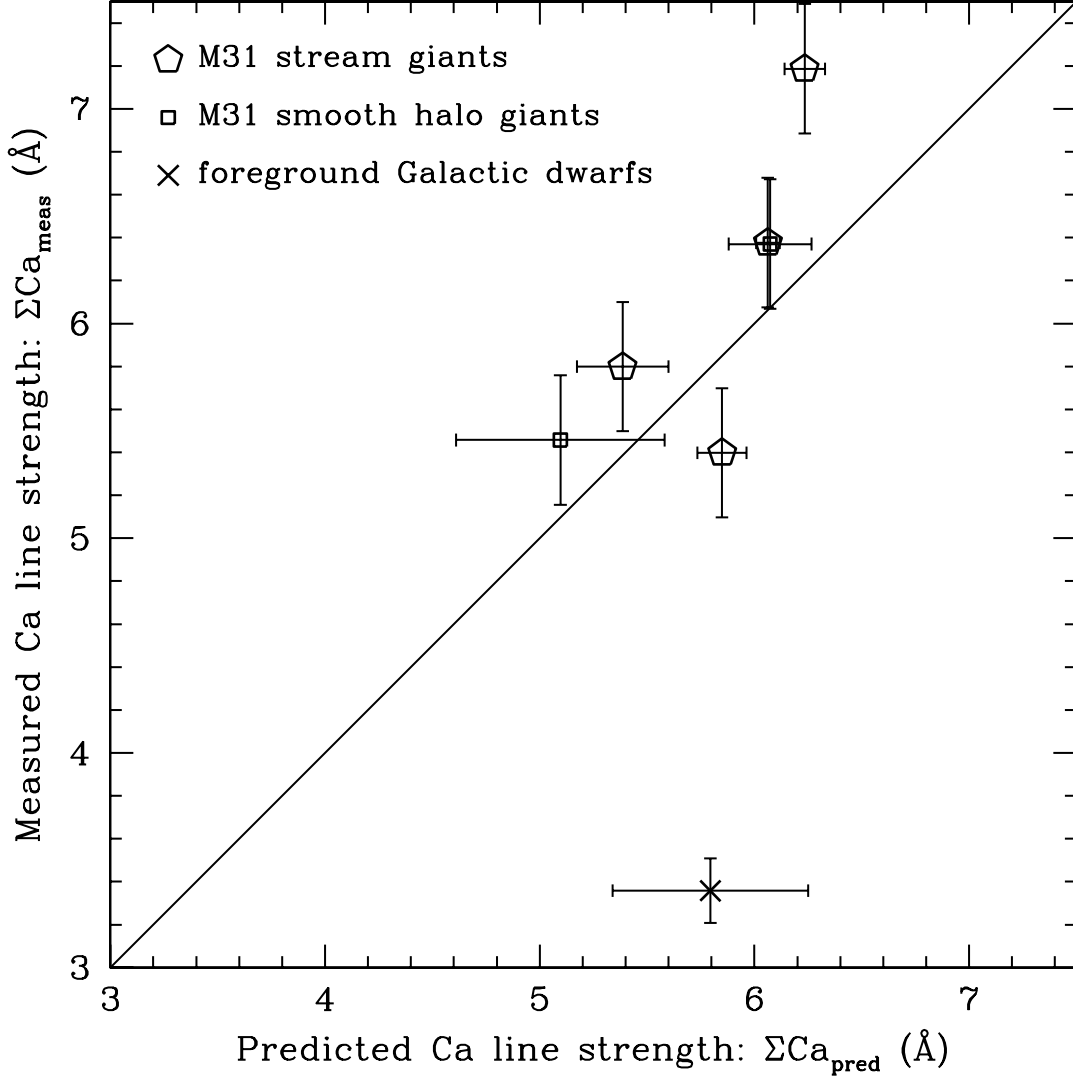


Fig. 12.— Measured equivalent width of the CaII triplet lines in coadded spectra plotted as a function of the predicted EW. The EW ΣCa is defined to be the weighted sum of the EWs of the three lines (§ 5.2.1). The $\Sigma\text{Ca}_{\text{pred}}$ value for each star is derived from its CMD/RGB fiducial-based metallicity estimate $[\text{Fe}/\text{H}]_{\text{phot}}$ and stellar luminosity, as described in the text. Stars are placed in groups of a dozen or more according to $\Sigma\text{Ca}_{\text{pred}}$ and their spectra coadded. M31 RGB stars in the giant southern stream (pentagons) and general halo (squares) show reasonable agreement between predicted and measured EWs, with the exception of the strongest-lined (most metal rich) stream stars for which $\Sigma\text{Ca}_{\text{meas}} > \Sigma\text{Ca}_{\text{pred}}$. The $\Sigma\text{Ca}_{\text{pred}}$ calculation makes no sense for foreground Galactic dwarf stars so it is no surprise that they fall well off the one-to-one relation (cross).